



HAL
open science

Identification of Durable and Non-Durable FeN_x Sites in Fe-N-C Materials for Proton Exchange Membrane Fuel Cells

Jingkun Li, Moulay Tahar Sougrati, Andrea Zitolo, James M Ablett, Ismail Can Oğuz, Tzonka Mineva, Ivana Matanovic, Plamen Atanassov, Ying Huang, Iryna Zenyuk, et al.

► **To cite this version:**

Jingkun Li, Moulay Tahar Sougrati, Andrea Zitolo, James M Ablett, Ismail Can Oğuz, et al.. Identification of Durable and Non-Durable FeN_x Sites in Fe-N-C Materials for Proton Exchange Membrane Fuel Cells. *Nature Catalysis*, 2020, 4, pp.10-19. 10.1038/s41929-020-00545-2 . hal-02931434v2

HAL Id: hal-02931434

<https://hal.science/hal-02931434v2>

Submitted on 2 Jan 2021

HAL is a multi-disciplinary open access archive for the deposit and dissemination of scientific research documents, whether they are published or not. The documents may come from teaching and research institutions in France or abroad, or from public or private research centers.

L'archive ouverte pluridisciplinaire **HAL**, est destinée au dépôt et à la diffusion de documents scientifiques de niveau recherche, publiés ou non, émanant des établissements d'enseignement et de recherche français ou étrangers, des laboratoires publics ou privés.

28
29 **Identification of durable and non-durable FeN_x sites in Fe-N-C materials for proton**
30 **exchange membrane fuel cells**

31

32 Jingkun Li¹, Moulay Tahar Sougrati¹, Andrea Zitolo², James M. Ablett², Ismail Can Oğuz¹,
33 Tzonka Mineva¹, Ivana Matanovic^{3,4}, Plamen Atanassov⁵, Ying Huang⁵, Iryna Zenyuk⁵,
34 Andrea Di Cicco⁶, Kavita Kumar⁷, Laetitia Dubau⁷, Frédéric Maillard⁷, Goran Dražić⁸ and
35 Frédéric Jaouen^{1*}

36 1 Institut Charles Gerhardt Montpellier, UMR 5253, CNRS, Université Montpellier, ENSCM,
37 Place Eugène Bataillon, 34095 Montpellier cedex 5, France

38 2 Synchrotron SOLEIL, L'orme des Merisiers, BP 48 Saint Aubin, 91192 Gif-sur-Yvette,
39 France

40 3 The Department of Chemical and Biological Engineering, Center for Micro-Engineered
41 Materials (CMEM), University of New Mexico, Albuquerque, NM 87131, USA.

42 4 Theoretical Division, Los Alamos National Laboratory, Los Alamos, NM 87545, USA

43 5 Department of Chemical and Biomolecular Engineering, National Fuel Cell Research
44 Center, University of California Irvine, Irvine, 92697, United States

45 6 School of Science and Technology, Physics Division, University of Camerino, 62032
46 Camerino (MC), Italy

47 7 Univ. Grenoble Alpes, Univ. Savoie Mont Blanc, CNRS, Grenoble INP[†], LEPMI, 38000
48 Grenoble, France

49 [†] Institute of Engineering Univ. Grenoble Alpes

50 8 Department of Materials Chemistry, National Institute of Chemistry, Hajdrihova 19, 1001
51 Ljubljana, Slovenia

52 * To whom correspondence should be addressed.

53 Email: frederic.jaouen@umontpellier.fr

54 **Abstract**

55 While Fe-N-C materials are a promising alternative to platinum for catalysing the oxygen
56 reduction reaction (ORR) in acidic polymer fuel cells, limited understanding of their
57 *operando* degradation restricts rational approaches towards improved durability. Here we
58 show that Fe-N-C catalysts initially comprising two distinct FeN_x sites (S1 and S2) degrade
59 *via* the transformation of S1 into iron oxides while the structure and number of S2 were
60 unmodified. Structure-activity correlations drawn from end-of-test ⁵⁷Fe Mössbauer
61 spectroscopy reveal that both sites initially contribute to the ORR activity but only S2
62 significantly contributes after 50 h of operation. From *in situ* ⁵⁷Fe Mössbauer spectroscopy in
63 inert gas coupled to calculations of the Mössbauer signature of FeN_x moieties in different
64 electronic states, we identify S1 to be a high-spin FeN₄C₁₂ moiety and S2 a low- or
65 intermediate-spin FeN₄C₁₀ moiety. These insights lay the ground for rational approaches
66 towards Fe-N-C cathodes with improved durability in acidic fuel cells.

67

68

69 Catalysis of the ORR is a cornerstone of industrially-relevant electrochemical
70 devices¹ that convert chemical energy into electric power (metal-air batteries,^{2,3} fuel cells
71 (FCs),^{2,4,5}) or electric power into high-added value products (H₂O₂,⁶⁻⁸ Cl₂ with oxygen-
72 depolarized cathodes⁹⁻¹¹). The pH in those devices establishes the ground for selecting
73 materials with promising ORR activity and durability. While proton exchange membrane FCs
74 (PEMFCs) are appealing,¹² their acidic environment is challenging. Platinum-based catalysts
75 now reach high activity and durability,^{13,14} but catalysts free of Pt-group-metals remain
76 topical for cost and sustainability reasons. Although metal-nitrogen-carbon (M-N-C) catalysts
77 (M=Fe, Co) have demonstrated high ORR activity,¹⁵⁻¹⁸ their durability in PEMFC is poor.
78 Their most active sites are atomically-dispersed MN_x moieties,^{15,16,18} and main degradation
79 mechanisms in acidic medium are demetallation,¹⁹⁻²³ surface carbon oxidation *via* Fenton
80 reactions,^{24,25} bulk carbon corrosion,^{21,26,27} and protonation of nitrogen groups followed by
81 anion adsorption — a phenomenon particularly important for Fe-N-C catalysts comprising
82 highly basic N-groups.²⁸ Exacerbated demetallation was recently reported in oxygenated acid
83 medium for highly-active NH₃-pyrolyzed Fe-N-C catalysts, explaining their poor durability
84 in PEMFC.^{22,29} The demetallation rate was measured online in acidic aqueous condition,²⁹ or
85 indirectly assessed by ⁵⁷Fe Mössbauer spectroscopy.²² In contrast, high stability in acidic
86 medium was reported by us for two catalysts exclusively comprising FeN_x moieties, with
87 only 25 % activity decrease after 30,000 load-cycles in Ar-saturated 0.1 M H₂SO₄ at 80°C.²¹
88 However, after 10,000 load-cycles in the same conditions but in O₂-saturated electrolyte, the
89 decrease in activity and number of FeN_x moieties was 65 and 83 %, respectively, forming
90 iron oxide particles during cycling.³⁰ Carbon corrosion was observed from Raman
91 spectroscopy after load cycles in O₂-saturated electrolyte,³⁰ while restricted changes in cyclic
92 voltammetry (restricted carbon corrosion) was observed by Dodelet *et al.* for an NH₃-
93 pyrolyzed Fe-N-C after a voltage hold of 6 h at 0.6 V in H₂/air PEMFC at 80°C.²²

94 Therefore, Fe-N-C catalysts comprising more of the durable FeN_x sites and less of the non-
95 durable ones should be targeted. Before the community can engage in this challenge, the
96 identification of which FeN_x sites are durable and which are not is required. It was revealed
97 with *ex situ* ⁵⁷Fe Mössbauer spectroscopy that Fe-N-C catalysts comprise two types of FeN_x
98 sites, labelled D1 (doublet with quadrupole splitting (QS) values of 0.9-1.2 mm·s⁻¹) and D2
99 (QS=1.8-2.8 mm·s⁻¹), both having a similar isomer shift (IS).^{15,31,32} By bridging density
100 functional theory calculations on QS-values with *ex situ* Mössbauer spectroscopy, we
101 identified D1 to be a high-spin Fe(III)N_x site (iron site S1) and D2 a low/medium-spin
102 Fe(II)N_x site (iron site S2),³³ in general agreement with two recent studies.^{34,35} While these
103 sites are ubiquitous in Fe-N-C catalysts, their respective activity and durability are unknown.

104

105 Here, we separately interrogate S1 and S2 with *in situ, operando* and end-of-test (EoT)
106 spectroscopies (see self-consistent definitions in Supplementary Note 1). With *in situ* ⁵⁷Fe
107 Mössbauer spectroscopy in O₂-free PEMFC, we demonstrate that a fraction of S1 is stable,
108 reversibly changing from high-spin ferric to high-spin ferrous state between 0.8 and 0.2 V,
109 while the electronic state of S2 is potential-independent, being ferrous low- or medium-spin.
110 *Ex situ* ⁵⁷Fe Mössbauer spectroscopy at 5 K after PEMFC potentiostatic operation reveals that
111 S2 is durable while S1 is not, with corresponding Fe cations forming ferric oxide
112 nanoparticles. We also provide evidence that S2 is the main contributor to ORR activity in
113 PEMFC after short operation time.

114

115

116 **Results**

117 ***Ex situ* characterization of pristine Fe-N-C catalysts**

118 This study was conducted on two Fe-N-C catalysts, previously demonstrated to be
119 free of iron clusters and containing only single-metal-atom FeN_x sites, synthesized as
120 previously reported (see Methods)¹⁵ and labelled Fe_{0.5} (pyrolysis in argon) and Fe_{0.5}-950(10)
121 (pyrolysis of Fe_{0.5} in NH₃ at 950 °C for 10 min). Their *ex situ* structure and morphology are
122 reported in Extended Data **Figure 1** and Supplementary **Table 1**, the main *ex situ* differences
123 between them being the higher surface basicity and microporous area of Fe_{0.5}-950(10). No Fe
124 particles were observed by transmission electron microscopy (TEM) in both pristine powder
125 catalysts, and the atomic-dispersion of Fe in Fe_{0.5} was further confirmed by STEM (Extended
126 Data **Figure 1g-i**). Their initial ORR activities in PEMFC (**Figure 1a**) are similar to values
127 reported in Ref.15 and representative for state-of-art Fe-N-C catalysts.^{18,22,36} NH₃ pyrolysis
128 introduces highly-basic nitrogen groups, increasing the turnover frequency (TOF) of FeN_x
129 sites but leading to decreased durability in PEMFC.^{15,17} This was recently explained by
130 higher demetallation rates for NH₃- vs. Ar-treated Fe-N-C catalysts in acid medium,^{17,29} while
131 demetallation rates were equally low in alkaline medium.²⁹ These results support the
132 involvement of highly basic nitrogen-groups in a significant fraction of FeN_x sites in Fe_{0.5}-
133 950(10), leading to higher TOF but also fast protonation of N-groups in acid medium, leading
134 to demetallation of the most active sites. Due to its high stability in acid,²¹ Fe_{0.5} was selected
135 for *in situ* ⁵⁷Fe Mössbauer spectroscopy in PEMFC. The *ex situ* Mössbauer spectra at 300 K
136 of Fe_{0.5} (powder) and Fe_{0.5}-cathode are identical, identifying only D1 and D2 (Extended Data
137 **Figure 2a-b**). However, one cannot exclude the formation of superparamagnetic ferric oxide
138 nanoparticles during cathode preparation, which would contribute with a doublet overlapping
139 with D1 signal from S1 sites.³⁷ To unveil this degeneracy, the spectra were acquired at lower
140 temperature (5 K), which increases the magnetization time constant of nano ferric-oxides,
141 contributing then with a sextet component,^{38,39} while the signal of S1 remains a doublet.⁴⁰ At
142 5 K, no sextet was visible for Fe_{0.5} while a broad sextet representing only 9 % of the

143 absorption area, assigned to superparamagnetic ferric oxide, appeared for Fe_{0.5}-cathode
144 (Extended Data **Figure 2c-d**). Thus, the low-QS doublet (labelled D1) in the Fe_{0.5}-cathode
145 spectrum at 300 K can mainly be assigned to S1 sites.

146

147 ***Operando* X-ray absorption spectroscopy of Fe_{0.5} in PEMFC**

148 *Operando* (extended) X-ray absorption near-edge and fine structure (XANES and
149 EXAFS, respectively) was acquired at Fe K-edge with fast acquisition mode in PEMFC (Cell
150 2,⁴¹ Supplementary **Figure 1a**, Supplementary Note 2). Reversible changes with
151 electrochemical potential were revealed (**Figure 1b**, Extended Data **Figure 3**), confirming in
152 PEMFC the *in situ* and/or *operando* XANES-EXAFS results previously measured in aqueous
153 acidic electrolyte for Fe_{0.5} and other catalysts comprising only/mostly FeN_x sites.^{2,16,42,43}
154 *Operando* XANES spectra indicate a Fe(III)/Fe(II) redox transition and conformational
155 changes of a significant fraction of FeN_x sites in the region 0.2-0.8 V (Extended Data **Figure**
156 **3a**), while *operando* EXAFS spectra indicate a change from an average O-Fe(III)N₄ to
157 Fe(II)N₄ coordination as the potential is decreased (Extended Data **Figure 3b**).⁴²⁻⁴⁴ The redox
158 transition is also seen by cyclic voltammetry in acid electrolyte and in line with the decreased
159 average oxidation state of Fe identified by the threshold energy of the XANES spectrum
160 (Extended Data **Figure 3c**).

161

162 ***In situ* Mössbauer spectroscopy of Fe_{0.5} in PEMFC**

163 X-ray absorption spectroscopies (XAS) however fail to provide separate information
164 on S1 and S2. To this end, we resorted to *in situ* ⁵⁷Fe Mössbauer spectroscopy with an in-
165 house single-cell PEMFC (Cell 3, Supplementary **Figure 1b**, Supplementary Note 2), whose
166 proper electrochemical response was verified (Supplementary **Figure 2**). The transmitted γ -
167 ray signal was continuously acquired for 36 h during each *in situ* potentiostatic experiments

168 at room temperature, with humidified H₂/argon at anode/cathode. Following the
169 potentiostatic controls shown in Extended Data **Figure 4**, we identified irreversible changes
170 in the Mössbauer spectra of Fe_{0.5}-cathode (during the first two cycles, discussed later) and,
171 thereafter, reversible changes triggered by the potential. **Figure 1c-d** shows reversible
172 changes for *in situ* Mössbauer spectra measured at 0.8 and 0.2 V during cycle 4, labelled 0.8
173 V (4) and 0.2 V (4). The hyperfine parameters IS and QS of D1 (labelled D1H for *in situ*
174 spectra, see later) and of D2 are similar at 0.8 V (4) to those measured *ex situ* for the pristine
175 Fe_{0.5}-cathode (Supplementary **Table 2**). In contrast, at 0.2 V (4), both the IS and QS values
176 for D1 (labelled D1L, see later) significantly increased, while those for D2 were unmodified
177 (**Figure 1d**, Supplementary **Table 2**, row “0.2 V (4)”). After all potential holds (Extended
178 Data **Figure 4**), we verified with *ex situ* Mössbauer spectroscopy at 5 K that the low-QS
179 doublet (labelled D1H and observed *in situ* at high potential in cycles 1-4) can still be
180 assigned to S1 sites (Supplementary **Figure 3**). D1H and D1L therefore represent the *in situ*
181 Mössbauer signal of S1 sites at high and low potential, respectively. **Figure 1c-d** also
182 identifies a third doublet D3, independent of potential and related to irreversible changes
183 occurring to the Fe_{0.5}-cathode during cycle 1 (discussed later).

184

185 We now discuss trends for all *in situ* Mössbauer spectra acquired at various potentials.
186 The spectrum 0.8 V (1) shows the doublets D1-D2 (Supplementary **Figure 4a**), with same IS
187 and QS values as those of the pristine Fe_{0.5}-cathode at 300 K (Extended Data **Figure 2b**).
188 However, the ratio D1/D2 is lower in 0.8 V (1) (Supplementary **Table 2**), indicating that
189 some unstable S1 sites were lost during the 36 h-long 0.8 V (1) experiment. From 0.8 V (1) to
190 0.2 V (1), the spectral parameters and intensity of D2 remained unchanged (Supplementary
191 **Figure 4a-b**). This applies also to all subsequent potential holds (Supplementary **Figures 5-**
192 **8**). In contrast, the signal from S1 at high potential (D1H) in 0.8 V (1) resulted in a much less

193 intense central doublet in 0.2 V (1) (grey doublet in Supplementary **Figure 4b**). This
194 indicates demetallation of a significant fraction of sites S1 during the first hold at 0.2 V, in
195 line with 15-40% activity loss after 10k load-cycles in inert gas reported by us for two Fe-N-
196 C catalysts (almost) exclusively comprising FeN_x sites.²¹ Since the 0.2 V (1) spectrum was
197 acquired for 36 h, it may be regarded as a time-averaged spectrum reflecting irreversible
198 phenomena. A detailed analysis of the time-dependence of 0.2 V (1) spectrum clearly reveals
199 this (Supplementary **Figure 9**, Supplementary Note 3). During cycles 2-4 however, the
200 switch between D1H and D1L was triggered solely by the electrochemical potential, with
201 distinct IS and QS values (**Figure 2a-b**, Supplementary **Figure 5b**). Regarding doublet D3
202 (IS~1.15·mm s⁻¹ and QS~2.5 mm·s⁻¹), it appeared first in 0.2 V (1) (Supplementary **Figure**
203 **4b**) and is unambiguously assigned to high-spin Fe²⁺ species due to its high IS.^{45,46} The
204 spectral parameters and intensity of D3 remained almost unchanged from 0.2 V (1) and
205 during all subsequent potential holds (**Figure 2e-f**, Supplementary **Figures 5-8**). From 0.8 V
206 (2) and afterwards, all spectral changes only reflect the reversible potential dependence of the
207 Mössbauer signature from S1 sites (**Figure 2**, Supplementary **Figures 5-7**). To gain
208 understanding on D3, we performed EoT Mössbauer spectroscopy of the Fe_{0.5}-cathode at
209 various temperatures, after completing all *in situ* measurements (Supplementary **Figures 3b**,
210 **10-11**, Supplementary **Table 3**, Supplementary Note 4). In summary, the *in situ* D3
211 component is assigned to high-spin Fe²⁺ cations (possibly complexed with Nafion® sulfonic
212 acid groups), formed from the demetallation of a fraction of S1 sites during 0.2 V (1)
213 (scheme in Extended Data **Figure 5**). When exposed to air, such cations form
214 superparamagnetic ferric oxide nanoparticles, overlapping then with D1 at 300 K
215 (Supplementary **Figure 10a-b**). At T ≤ 80 K, they however then contribute with a sextet
216 component with IS and hyperfine magnetic field corresponding to ferric oxide
217 (Supplementary **Figure 10b-f**). A summary of the inter-relation between the Mössbauer

218 components *ex situ*, *in situ*, and EoT after *in situ* measurements is given in Supplementary
219 **Table 4**.

220

221 **Reversibly-changing *in situ* coordination of S1 with potential**

222 We now discuss the structures and electronic states of S1 and S2. The *in situ* (absence
223 of O₂) Mössbauer signal of the fraction of S1 sites that survived 0.2 V (1) reversibly switches
224 between D1L at 0.2 V and D1H at 0.8 V (**Figure 2a-b**). D1H is identical to D1 measured *ex*
225 *situ* on pristine Fe_{0.5}, that we recently identified to be mainly Fe(III)N₄C₁₂ periodic or cluster
226 structures in high-spin state, with axial oxygen adsorbates.^{33,42} Due to its high IS-value, the
227 assignment of D1L to a high-spin Fe(II) species is straightforward.^{45,46} Consequently, only a
228 restricted change in the average iron-spin is expected for Fe_{0.5}-cathode between high and low
229 potential. We used a three-electrode cell (Cell 4,¹⁶ Supplementary **Figure 1c**, Supplementary
230 Note 2) to verify this with *in situ* Fe K_β X-ray emission spectroscopy (XES), a technique
231 well-suited to investigate the spin-state of metal centers.⁴⁷ The overlapping *in situ* XES
232 spectra at 0.2 and 0.8 V support that the sites S1 are in high-spin at all potentials
233 (Supplementary **Figure 12**). The switch from D1H to D1L signal for S1 is thus the outcome
234 of the reduction from Fe(III)N₄C₁₂ to Fe(II)N₄C₁₂, also triggering the removal of an axial
235 OH-adsorbate. To further support this, we applied our recently reported DFT methods³³ to
236 calculate the QS-value of different high-spin OH-Fe(III)N₄C₁₂, OH-Fe(III)N₄C₁₀, Fe(II)N₄C₁₂
237 and Fe(II)N₄C₁₀ models (Supplementary **Figure 13**, the atomic coordinates of the optimised
238 models are provided in Supplementary **Data 1**). While high-spin OH-Fe(III)N₄C₁₂ and OH-
239 Fe(III)N₄C₁₀ structures lead to QS-values of 0.6-1.0 mm·s⁻¹, matching those of D1H, only the
240 high-spin Fe(II)N₄C₁₂ structures lead to QS-values of 1.7-2.0 mm·s⁻¹, matching those of D1L
241 (Supplementary **Table 5**). The QS-values of high-spin Fe(II)N₄C₁₀ structures are >3.0 mm·s⁻¹,
242 significantly higher than those of D1L (Supplementary **Table 5**). These results confirm our

243 recent assignment of D1 to high-spin Fe(III)N₄C₁₂ structures with axial oxygen ligand,³³ and
244 reveal their switch to high-spin Fe(II)N₄C₁₂ structures, without axial ligand, at low potential
245 (D1L). *Operando* EXAFS spectra (Extended Data **Figure 3b**) also support that the Fe(III)-to-
246 Fe(II) reduction is accompanied by desorption of oxygen adsorbates.^{42,48} This redox switch is
247 in line with *in situ/operando* XAS on numerous Fe-N-C catalysts^{2,16,42,43} and with the
248 significant presence of S1 in Fe-N-C catalysts.^{15,31,32,42} Here, we show that S1 undergoes this
249 redox transition, but not S2. We then analysed the potential-dependence of the S1 hyperfine
250 parameters. **Figure 3a-b** shows that they can be divided into those below 0.5 V and those
251 above (D1L and D1H, respectively). For comparison, **Figure 3c** reports the DFT-calculated
252 QS for high-spin OH-Fe(III)-N₄C₁₂ and high-spin Fe(II)-N₄C₁₂ structures, demonstrating that
253 our DFT method correctly reproduces the change in QS. Supplementary **Table 4** summarises
254 the main findings on D1H and D1L and how they inter-relate with the site S1.

255

256 **Different fates of sites S1 and S2 in an operating PEMFC**

257 We then attempted to investigate the electronic states and durability of S1 and S2 with
258 *operando* (O₂) Mössbauer spectroscopy. However, this proved impossible for S1. After a
259 single potential hold at 0.2 V in O₂, no S1 sites were observed in the EoT Mössbauer
260 spectrum at 5 K while two sextets appeared, assigned to ferric oxide particles (Extended Data
261 **Figure 6c**). The relative amount of sextets is much higher than in the pristine Fe_{0.5}-cathode
262 (Extended Data **Figure 6a**), supporting that the major fraction of S1 sites survived the MEA
263 preparation, but transformed to ferric oxides during fuel cell testing. The cathode was also
264 characterized before and after the potential hold with TEM (Extended Data **Figure 6b,d**) and
265 XRD (Extended Data **Figure 6e**). Only TEM after operation identified Fe particles of *ca* 5-15
266 nm size. The *operando* Mössbauer spectra were comparable at OCP and 0.2 V (not shown)
267 which, combined with the EoT spectrum at 5 K, suggests that the D1-like signal identified at

268 0.2 V under *operando* conditions already originated from ferric oxides instead of S1 sites.
269 The presence of ferric oxides at 0.2 V in turn suggests those particles are not electronically
270 connected to the cathode, but only in contact with Nafion phase. In contrast, the parameters
271 and absolute intensity of D2 were unmodified before and after 0.2 V hold in O₂
272 (Supplementary **Table 6**). This indicates that the electronic state of S2 is potential-
273 independent in the range 0.2-0.9 V and independent of the presence/absence of O₂. This in
274 turn indicates that S2 is either not accessible to O₂ or binds O₂ weakly, in line with our *ex situ*
275 analysis.³³ The activity of Fe_{0.5}-cathode before and after *operando* measurements (Cell 3) was
276 measured in Cell 1 at 80°C. A restricted ORR-activity decrease from 23 to 15 mA·cm⁻² is
277 observed at 0.8 V (Extended Data **Figure 6f**). The remaining activity is much higher than that
278 of the Fe-free N-doped carbon matrix (N-C),¹⁵ implying that either S2 or ferric oxides are
279 active. To evaluate the ORR activity of the latter, we precipitated Fe₂O₃ nanoparticles on the
280 same N-C support. The activity of Fe₂O₃/N-C above 0.7 V is within reproducibility equal to
281 that of N-C, implying no or negligible ORR activity of Fe₂O₃ (Supplementary **Figure 14**).

282

283 To follow spectral changes as a function of operating time, a series of cathodes was
284 prepared from a same Fe_{0.5} batch and operated at 0.5 V in Cell 1 for either 5, 10, 25 or 50 h.
285 Polarisation curves were recorded before and after each experiment. Each MEA was
286 characterized with EoT ⁵⁷Fe Mössbauer spectroscopy at 5 K (**Figure 4a-c**, Supplementary
287 **Figure 15**, Supplementary **Table 7**). The fittings indicate unmodified spectral parameters and
288 absolute intensity for D2 with operation time, continuously decreasing signal intensity for D1
289 and continuously increasing signal intensity for the two sextets, assigned to
290 superparamagnetic ferric oxide (**Figure 4a-c**, Supplementary **Figure 15**). EoT XANES
291 reveals only minor changes (Supplementary **Figure 16a**) while EXAFS spectra after 10-50 h
292 reveal a small increase in the Fe-Fe signal at ~2.7 Å, matching the Fe-Fe distance in Fe₂O₃

293 (Supplementary **Figure 16b**). X-ray computed tomography performed *ex situ* after 50 h of
294 operation at 0.5 V shows the presence of Fe particles (**Figure 4e**, Supplementary **Figure 17a**).
295 Most particles are present on or near the outer surface of the N-C matrix. Size distribution
296 analysis (Supplementary **Figure 17b**) reveals the presence of particles 5 to 60 nm in size,
297 with the most frequent sizes being between 5 and 10 nm (47.5%). The initial and final
298 polarisation curves indicate a sharp activity decrease after 5 h operation at 0.5 V followed by
299 a slow but steady activity decrease (**Figure 4d**, Supplementary **Figure 18a**).

300

301 **Evidence for ORR activity contributions from S1 and S2 sites**

302 To identify structure-activity relationships, we plotted the absolute area of each
303 spectral component and the current density at 0.8 V as a function of time (**Figure 5a-d**). The
304 results indicate a trend of decreased activity with operation time, decreasing amount of sites
305 S1, increasing amount of ferric oxides (sextets) and unchanged amount of sites S2. Based on
306 this, we plotted in **Figure 5e** the current density at 0.8 V as a function of the absolute
307 absorption area for either D1 or (D1+D2). Except for the initial activity measurements, the
308 results reveal a linear correlation between the activity and either D1 or (D1+D2),
309 demonstrating that S1 contributes to ORR activity. The data for the initial activity (star
310 symbol) is an outlier and this can be explained by a higher TOF of Fe-based sites during the
311 first polarisation curve. This hypothesis is in line with our recent work that demonstrated
312 decreased TOF of Fe-based sites by chemical reaction of Fe_{0.5} with H₂O₂.²⁵ The activity drop
313 from 0 to 5 h of operation is thus assigned to both decreased TOF *via* mild surface oxidation
314 of carbon (vertical arrows in **Figure 5e**), and decreased number of S1 sites (arrows along the
315 dashed lines in **Figure 5e**). After 5 h operation, the TOF of the Fe sites seems stabilized,
316 leading to linear correlations between the overall activity and either D1 or D1+D2. The
317 extrapolation at $x = 0$ of the plot of activity *vs.* absolute area of D1 leads however to a

318 positive y-intercept, indicating that the $\text{Fe}_{0.5}$ -cathode should have a significant ORR activity
319 even in the absence of S1. This is supported by the results after operation at 0.2 V in O_2
320 (Extended Data **Figure 6**). In contrast, the extrapolation at $x = 0$ of the plot of activity vs.
321 absolute area of D1H+D2 is near zero, supporting the fact that both S1 and S2 are ORR-
322 active in acidic medium. A rigorous analysis shows that this near-zero y-intercept can be
323 interpreted either as S2 sites being all located on the surface and having a similar TOF as S1,
324 or only a fraction of S2 sites are on the surface and implying then a higher TOF than S1
325 (Supplementary Note 5). From EoT Raman spectroscopy, no carbon corrosion was identified
326 (Supplementary **Figure 18b**). We verified that these trends also apply to the initially more
327 active $\text{Fe}_{0.5}$ -950(10) catalyst (Extended Data **Figure 7**, Supplementary **Table 8**, and
328 Supplementary **Note 6**). The relative % area of D1 decreased from 32 to 6 % during 50 h at
329 0.5 V for $\text{Fe}_{0.5}$ -950(10) and from 43 to 6% for $\text{Fe}_{0.5}$. For D2, the relative % area decreased
330 from 40 to 38 % in 50 h for $\text{Fe}_{0.5}$ -950(10) but slightly increased from 49 to 51 % for $\text{Fe}_{0.5}$.
331 The variation of ± 2 % in D2 is within the error, and D2 can be considered durable in both
332 cathodes. Comparative STEM-EDX analysis of $\text{Fe}_{0.5}$ -950(10) fresh and aged (50 h at 0.5 V)
333 cathodes identify few large Fe particles in the fresh cathode but numerous Fe nanoparticles
334 after aging (Supplementary **Figure 19**). In addition, the correlation between Fe and F
335 mapping in the aged cathode suggests that Fe clustering is linked to the presence of Nafion
336 ionomer (Supplementary **Figure 20**).

337

338 **Conclusions**

339 In conclusion, we identify with Mössbauer spectroscopy the high-spin S1 site and the
340 low- or intermediate-spin S2 site, both assigned to FeN_4 moieties but embedded in different
341 ways in the carbon matrix. Iron in the site S1 switches oxidation state III/II in the region 0-1
342 V while S2 does not, remaining Fe(II). We also identify that both sites initially contribute to

343 the ORR activity of Fe-N-C in acidic medium. However, S1 is not durable in operating
344 PEMFC, quickly transforming to ferric oxides (**Figure 6**). In contrast, S2 is shown to be
345 more durable, with no measurable decrease of the number of active sites after 50 h operation
346 at 0.5 V. The lack of change of oxidation state for Fe in S2 in the region 0-1 V is not
347 contradictory with catalysis. For example, we showed with *in situ* XAS that CoN_x sites do not
348 change oxidation state in acidic medium in the same region but catalyze ORR.^{16,44} The
349 degradation of S1 into ferric oxides may be a direct or indirect demetallation, the indirect
350 pathway possibly triggered by localized carbon surface oxidation or protonation of highly
351 basic nitrogens involved in S1. The stability of S2 may be due to a more graphitic local
352 structure, lower amount of reactive oxygen species (ROS) produced during ORR in acid, or
353 its sub-surface location activating the N-doped carbon top-surface. These results and/or
354 methods are of high interest to the improved understanding of Fe-N-C materials for
355 application in PEMFC but also in anion-exchange membrane fuel cells and for CO₂ electro-
356 reduction.⁴⁹⁻⁵⁰ For PEMFC application, further efforts should be devoted to increasing the site
357 density of S2 sites and/or to stabilize S1 in acidic and oxygenated environment. The former
358 goal might be achieved by depositing a thin overlayer of N-doped carbon on top of Fe-N-C
359 (possibly transforming S1 into S2 sites) and the latter goal by adding co-catalysts (to
360 scavenge H₂O₂ or ROS formed during ORR in acid medium) or by integrating S1 sites in a
361 more graphitic carbon support. In addition, the targeted removal of sites S1 before integrating
362 Fe-N-C materials in PEMFC cathodes would avoid the formation of ferric oxides under
363 *operando* conditions, in turn likely forming ROS in the presence of H₂O₂.

364

365
366
367 **Figure 1. Initial activity and reversible spectral changes of Fe with PEMFC potential. (a)**
368 PEMFC Tafel plots of Fe_{0.5} and Fe_{0.5}-950(10); **(b)** Fe K-edge XANES spectra measured
369 under *operando* conditions in PEMFC as a function of potential; *in situ* ⁵⁷Fe Mössbauer
370 spectra at 0.8 V **(c)** and 0.2 V **(d)** acquired during the fourth cycle. For **(a)**, the cell
371 temperature was 80 °C, the flow rates of O₂ and H₂ were 60 sccm with 100% relative
372 humidity, the gauge pressure was 1 bar and the cathode loading was 4 mg·cm⁻². For **(b)**, all
373 the testing conditions were the same as **(a)**, except that no backpressure was applied. For **(c-**
374 **d)**, the cell was at room temperature, the humidifiers were at 50 °C, Ar and H₂ gases were fed
375 at cathode and anode respectively, and no backpressure was applied. Each Mössbauer
376 spectrum was collected for 36 hours. D1H is the Mössbauer signature of S1 sites at high
377 potential while D1L is their signature at low potential.

378

379

380

381 **Figure 2. Effect of PEMFC potential on doublets from fitted *in situ* Mössbauer spectra.**
382 The spectral doublet D1 **(a)**, D2 **(c)** and D3 **(e)** resulting from the fittings, and the
383 corresponding IS and QS values of D1 **(b)**, D2 **(d)** and D3 **(f)** at 0.8 V (2), 0.2 V (2), 0.8 V (4)
384 and 0.2 V (4). The number in parentheses represents the cycle number. In **(a)**, **(c)** and **(e)**,
385 solid curve: 0.8 V (2); dashed curve: 0.2 V (2); ×: 0.8 V (4); ∴: 0.2 V (4). In **(b)**, **(d)** and **(f)**, □:
386 QS; ●: IS. D1H is the Mössbauer signature of S1 sites at high potential while D1L is their
387 signature at low potential. The experimental spectra and all fitted components from which the
388 **Figures 2a, 2c** and **2e** were made can be seen in Supplementary **Figure 6**.

389

390

391 **Figure 3. Experimental and calculated values of hyperfine parameters vs. potential.**

392 Reversible change of IS- **(a)** and QS-values **(b)** of the spectral component D1 vs.
393 electrochemical potential. The error bars in **(a)** and **(b)** at 0.8 and 0.2 V represent the standard
394 deviation from three separate measurements on different cycles. **(c)** The QS-values calculated
395 with PBE/DZVP2 method for different $\text{FeN}_4\text{C}_{12}$ model structures in high-spin, with/without
396 oxygen adsorbate. The structures 1e, 1f and 2e are given in Supplementary **Figure 13**. QS-
397 values calculated for $\text{FeN}_4\text{C}_{10}$ model structures are given in Supplementary **Table 5**.

398

399

400 **Figure 4. Characterisation of $\text{Fe}_{0.5}$ -cathode after operation at 0.5 V in PEMFC. (a) *Ex***

401 *situ* ^{57}Fe Mössbauer spectrum at 5 K of the pristine $\text{Fe}_{0.5}$ -cathode. EoT Mössbauer spectra at

402 5 K of the $\text{Fe}_{0.5}$ -cathode after a hold at 0.5 V for 5 h **(b)** and 50 h **(c)**. **(d)** The corresponding

403 Tafel plots. The inset in **(a)**, **(b)** and **(c)** shows the Tafel plot trace, the thicker curve

404 corresponding to each spectrum. The cell temperature was 80 °C, 60 sccm O_2 and H_2 gases

405 with 100% relative humidity were fed at cathode and anode respectively, the gauge pressure

406 was 1 bar, and the cathode loading was $4 \text{ mg}\cdot\text{cm}^{-2}$. **(e)** Volume-rendered FeO_x particles (left)

407 and FeO_x particles superimposed onto the morphology of support material (right) of the $\text{Fe}_{0.5}$ -

408 cathode after a hold at 0.5 V for 50 h, obtained from X-ray computed tomography with phase

409 contrast for soft elements (mainly C and N) and absorption contrast for hard elements (*i.e.*

410 Fe).

411

412

413 **Figure 5. Correlations between FeN_x site amount in Fe_{0.5}-cathode and activity over time.**

414 (a) Current density of the Fe_{0.5}-cathode at 0.8 V vs. duration of operation at 0.5 V in H₂/O₂

415 PEMFC, absolute absorption areas of D1 (b), D2 (c) and sextets (d) vs. duration of operation

416 at 0.5 V in H₂/O₂ PEMFC. (e) The current density of Fe_{0.5}-cathodes at 0.8 V as a function of

417 the absolute absorption area for D1 and D1+D2. The absolute absorption area of a given

418 spectral component is proportional to the number of corresponding sites in the cathode.

419

420

421

422

423

424 **Figure 6. Coordination or structural changes of the sites S1 and S2 under *in situ* or**

425 ***operando* conditions.** The site S1 is a high-spin FeN₄C₁₂ structure, undergoing reversible

426 change of Fe oxidation state from III to II *in situ* (no O₂) for the most stable S1-sites fraction

427 (D1H to D1L double-sided black arrow), while the less stable fraction of S1 sites irreversibly

428 transforms *in situ* into high spin Fe²⁺ (D1H to D3, single-sided black arrow). When exposed

429 to ambient air for EoT measurement following the *in situ* measurement, high spin Fe²⁺

430 transform into ferric oxides (D3 to Fe₂O₃, single-side red arrow). S1 sites irreversibly

431 transform into ferric oxides under *operando* conditions when catalysing the ORR (single-

432 sided red arrow), most probably *via* a fast intermediate stage involving the leaching of Fe²⁺

433 cations (D3) before the oxide growth may start. S2 sites do not change oxidation state and are

434 stable both *in situ* and *operando* (double-sided arrows).

435

436 **Methods**

437 **Synthesis.** The synthesis of Fe_{0.5} and Fe_{0.5}-950(10) was reported previously.¹⁵ Catalyst
438 precursors were prepared from a Zn(II) zeolitic imidazolate framework (Basolite Z1200 from
439 BASF, labelled ZIF-8), Fe(II) acetate (Fe(II)Ac), and 1,10-phenanthroline (Phen). ⁵⁷Fe(II)Ac
440 was used as iron precursor for all Mössbauer studies. For *operando* XAS, natural Fe(II)Ac
441 was used. The catalyst Fe_{0.5} was synthesized via the dry ball-milling of ZIF-8 (800 mg), Phen
442 (200 mg) and Fe(II)Ac (16 mg) in a zirconium oxide crucible filled with 100 zirconium oxide
443 balls (5 mm diameter) at 400 rpm for 2 hours (Fritsch Pulverisette 7 Premium, Fritsch, Idar-
444 Oberstein, Germany). The subscript in Fe_{0.5} corresponds to the Fe content (wt %) in the entire
445 catalyst precursor before pyrolysis. Then the mixed precursor was pyrolyzed in flash mode in
446 Ar at 1050 °C for 1 hour. Owing to a mass loss of 65–70 wt % during pyrolysis in Ar, caused
447 by volatile products formed from ZIF-8 and Phen, the iron content in Fe_{0.5} is about three
448 times the iron content in the catalyst precursor. Fe_{0.5} was subjected to a second flash pyrolysis
449 for 10 min at 950 °C in NH₃, yielding Fe_{0.5}-950(10). The mass loss of carbon during NH₃
450 pyrolysis was 25–31%, further increasing the iron content.

451 To synthesize Fe₂O₃/N-C, the Fe-free N-C was firstly synthesized identically with Fe_{0.5}-950
452 except for the first ball-milling step, where no Fe(II)Ac was added. Then 15 mg of
453 FeCl₂·4H₂O was dissolved in 7.5 mL H₂O/ethanol solution (v:v=24:1). Then 300 mg N-C
454 was added, and well-mixed *via* sonication for 1 hour. The obtained slurry was stirred
455 continuously for another 48 hours, followed by filtration, washing with water, and dry in the
456 oven at ~50 °C overnight. The Fe₂O₃/N-C sample was obtained by a final heat treatment at
457 200 °C for 2 hours in Ar with a ramping rate of 5 °C·min⁻¹. The Fe content in Fe₂O₃/N-C was
458 found to be 1.3 wt.% by X-ray fluorescence (XRF) spectroscopy.

459 **XRF.** The metal content in Fe₂O₃/N-C was measured *via* X-ray XRF spectroscopy (Axios
460 Max from PANalytical, Netherlands). Fe₂O₃/N-C powder was mixed with boric acid as a

461 binder in a ratio of 1:3 by weight *via* ball-milling at 400 rpm for 30 min. Then 200 mg of the
462 mixture was pelletized as a disk of 13 mm diameter for XRF measurements. The calibration
463 curve was performed using 0.1, 0.2, 0.5, 1.0, 1.5 and 2.0 wt% Fe in a mixture of Fe(II)Ac and
464 Vulcan XC72R. The Vulcan XC72R (mixed with Fe(II)Ac) were mixed with boric acid in a
465 ratio of 1:3 by weight *via* ball-milling at 400 rpm for 30 min, and then 200 mg of the mixture
466 was pelletized as a disk of 13 mm diameter.

467 **XRD.** X-ray diffraction patterns were recorded using a PANanalytical X'Pert Pro powder X-
468 ray diffractometer with Cu K α radiation.

469 **STEM.** Probe Cs-corrected scanning transmission electron microscope Jeol ARM 200 F,
470 equipped with a cold field emission electron source, was used for imaging atomically-
471 dispersed FeN $_x$ C $_y$ moieties in Fe $_{0.5}$ pristine powder. To minimize the beam damage, 80 keV
472 and low beam current were used. High-angle annular dark-field (HAADF) images were
473 obtained using 68-180 mrad collection half-angles at 24 mrad probe convergence semi-angle.
474 Images were filtered with non-linear filter which is a combination of low-pass and Wiener
475 filters. The presence of iron and nitrogen was confirmed with Gatan Quantum ER dual
476 Electron Energy-loss Spectroscopy system.

477 **TEM and STEM-EDX.** A JEOL 2010 Transmission Electron Microscopy operated at 200
478 kV was used to examine Fe-N-C cathodes before testing or at EoT. The resolution was 0.19
479 nm. Elemental mapping was performed on fresh/aged Fe $_{0.5}$ -950(10) cathode using a 200 kV
480 JEOL 2100F microscope equipped with a retractable large angle Centurio Silicon Drift
481 Detector (SDD) detector. The Fe *K*, C *K* and O *K* lines and the *K*-factors specified by the
482 JEOL software were used for elemental quantification.

483 **Raman spectroscopy.** Raman spectra were collected using a LabRAM ARAMIS Raman
484 microscope with a 473 nm laser.

485 **N₂ sorption isotherms acquisition and analysis.** N₂ adsorption/desorption was performed at
486 liquid nitrogen temperature (77 K) with a Micromeritics ASAP 2020 instrument. Prior to the
487 measurements, all samples were degassed at 200 °C for 5 h in flowing nitrogen to remove
488 guest molecules or moisture. The pore size distributions were calculated by fitting the full
489 isotherm with the quench solid density functional theory model with slit pore geometry from
490 NovaWin (Quantachrome Instruments).

491 **Basicity measurement of pristine Fe-N-C powders.** The basicity measurement of Fe_{0.5} and
492 Fe_{0.5}-950(10) has been reported elsewhere.¹⁵ A solution with pH 6.0 was first prepared by the
493 titration of a 0.1 M H₂SO₄ solution by 0.1 M KOH. Then 40 mg catalyst was dispersed into
494 20 ml aqueous solution with an initial pH (pH_i) of 6.0. The solution was constantly saturated
495 with N₂ to avoid acidification from air. The final pH (pH_f) after the dispersion of the catalyst
496 was measured once the pH meter indicated a stable value.

497 **Electrochemical characterisation.** The ORR activities of Fe_{0.5} and Fe_{0.5}-950 were
498 investigated in a single-cell PEMFC (Cell 1, see also Supplementary Note 2). For the
499 membrane electrode assembly (MEA), cathode inks were prepared by sonicating for 1 hour
500 the mixture of 20 mg of catalyst, 652 µL of a 5 wt% Nafion solution containing 15–20%
501 water, 326 µL of ethanol and 272 µL of de-ionized water. Then, three aliquots of 405 µl of
502 the catalyst ink were successively deposited on the microporous layer of a 4.84 cm² gas
503 diffusion layer (Sigracet S10-BC). The cathode was then placed at 60 °C to dry for 2 hours.
504 The anode used for all PEMFC tests in Cell 1 was 0.5 mg_{Pt}·cm⁻² on Sigracet S24-BC. Nafion
505 NRE-211 was used as membrane. No hot-pressing was applied in order to easily peel off the
506 cathode for EoT characterisation. PEMFC tests were performed with a single-cell fuel cell
507 with serpentine flow field (Fuel Cell Technologies) using an in-house test bench and a
508 Biologic potentiostat with a 50 A load and EC-Lab software. The fuel cell temperature was
509 80 °C, the humidifiers were set at 85 °C and the inlet pressures were set to 1 bar gauge for

510 both anode and cathode sides. The flow rate for humidified H₂ and O₂ gases was 60 sccm
511 downstream. No break-in was applied before recording the first polarisation curve.
512 Polarization curves were recorded by scanning the voltage at 1 mV·s⁻¹.

513 ***Ex situ* and *operando* XAS.** Fe K-edge X-ray absorption spectra were collected at room
514 temperature at SAMBA beamline (Synchrotron SOLEIL). The beamline is equipped with a
515 sagittally focusing Si 220 monochromator, and X-ray harmonics are removed by two Pd-
516 coated mirrors. For *ex situ* measurements on pristine Fe-N-C catalysts, the powders were
517 pelletized as disks of 10 mm diameter with 1 mm thickness, using Teflon powder (1 μm
518 particle size) as a binder and XAS measured in transmission mode. For *ex situ* measurements
519 on Fe-N-C cathodes (before testing or at EoT), XAS was acquired in fluorescence mode. For
520 *operando* XAS experiments, MEAs were prepared identically as for measurements in the
521 commercial PEMFC (Cell 1). The design of the PEMFC used for *operando* XAS study (Cell
522 2, see also Supplementary Note 2) was reported in Ref. 41. The cell temperature was 80 °C,
523 60 sccm O₂ and H₂ with 100% relative humidity were fed at cathode and anode respectively,
524 and the cathode loading was 4 mg·cm⁻². No backpressure was applied.
525 *Operando* measurements were performed by recording the Kα X-ray fluorescence of Fe with
526 a Canberra 35-elements monolithic planar Ge pixel array detector.

527 ***Ex situ* and *in situ* Mössbauer spectroscopy.** ⁵⁷Fe-enriched Fe(II)Ac was used as iron
528 precursor for all Mössbauer studies. The ⁵⁷Fe Mössbauer spectrometer (Wissel, Germany)
529 was operated in transmission mode with a ⁵⁷Co: Rh source. The velocity driver was operated
530 in constant acceleration mode with a triangular velocity waveform. The velocity scale was
531 calibrated with the magnetically split sextet of a high-purity α-Fe foil at room temperature.
532 The spectra were fitted to appropriate combinations of Lorentzian profiles representing
533 quadrupole doublets, sextets by least-squares methods. IS values are reported relative to α-Fe
534 at room temperature. Unless otherwise mentioned in the Supplementary **Tables 2, 3, 6-8**, the

535 fittings were performed with unconstrained parameters (relative area, IS, QS, LW, H) for
536 each spectral component. For *ex situ* measurements on pristine Fe-N-C catalysts, powders
537 (20-30 mg) were mounted in a 2 cm² holder. For *ex situ* measurements on Fe-N-C cathodes,
538 before testing or at EoT, 5 cm² electrodes were cut into four pieces and stacked on each other.
539 Mössbauer measurements below 100 K were performed in a helium flow cryostat (SHI-850
540 Series from Janis, USA). For *in situ* Mössbauer experiments, MEAs were prepared as
541 described for testing in the commercial PEMFC (Cell 1), except that the anode was 0.1 mg_{Pt}
542 cm⁻² to maximize γ -ray transmission through the cell. The design of the PEMFC for *in situ*
543 Mössbauer spectroscopy (Cell 3, see also Supplementary Note 2) is shown in Supplementary
544 **Figure 1b**. The cell was at room temperature, the humidifiers were at 50 °C, Ar and H₂ gases
545 were fed at cathode and anode respectively, and no backpressure was applied. The Mössbauer
546 signal was continuously acquired for 36 hours at each cathode potential.

547 ***In situ* XES.** Fe K _{β} X-ray emission spectra were collected at room temperature using a 1m
548 radius Germanium 620 analyzer crystal at GALAXY inelastic scattering end-station
549 (Synchrotron SOLEIL).⁵¹⁻⁵² The incident energy was 8500 eV (using a silicon double-crystal
550 monochromator) and the focused beam size was 30 [ver.] x 90 [hor.] μm^2 . The sample,
551 analyser crystal and silicon drift detector were all arranged in a vertical Rowland circle
552 geometry and air absorption was reduced by using helium flight paths. The electrochemical
553 cell (Goodfellow cat. C 000200/2) used for *operando* XES in liquid electrolyte with a three
554 electrode system is the same as the one previously for *in situ* or *operando* XAS
555 measurements (Cell 4, see also Supplementary Note 2).¹⁶ Catalyst inks were prepared by
556 mixing 10 mg catalyst with 50 μL de-ionized water and 100 μL of 5 wt% Nafion® solution
557 with ultrasounds. A 50 μL aliquot was then pipetted on $\sim 3\text{ cm}^2$ circular area of a 100- μm -
558 thick graphite foil, resulting in a catalyst loading of $\sim 1\text{ mg}\cdot\text{cm}^{-2}$. The graphite foil with
559 deposited catalyst then served as a working electrode, Ag/AgCl and Pt were used as reference

560 and counter electrodes, respectively. The cell was filled with 0.5 M H₂SO₄ and saturated with
561 N₂ by continuously bubbling gas in the electrolyte.

562 **X-ray computed tomography (CT).** X-ray CT imaging was performed at the Advanced
563 Photon Sources (APS) at Argonne National Laboratory (ANL) using Beamline 32-ID, with 8
564 keV energy and 0.4 s exposure time. Fresnel zone plates with grading of 44.6 nm were used
565 to achieve resolution of 44.6 nm. Zernike phase contrast was used to detect soft elements,
566 whereas absorption contrast was used for imaging hard materials. Image phase retrieval and
567 reconstructions were performed using TomoPy.⁵³ The volume-rendering structure and
568 analysis were done in Dragonfly 4.1.⁵⁴ The calculated volume-to-surface area ratio was
569 considered as the sizes of the particles. The surface area was calculated by pixel-wise method.

570 **DFT computation.** Density functional theory (DFT) spin-polarized calculations were carried
571 out with the cluster and periodic approaches using respectively, deMon2k.6.0.2 developers
572 version^{55,56} and VASP^{57,58} computer programs on graphene sheets (with defects) integrating
573 various moieties from the ferrous and ferric FeN₄C₁₀ and FeN₄C₁₂ sub-groups. The
574 considered cluster and periodic models are reported in Supplementary **Figure 13**. The
575 dangling bonds in all structures were saturated with hydrogen atoms. In the cluster
576 calculations, the electrons of the C, H and N atoms are described by triple- ξ basis set and of
577 Fe by double- ξ plus polarization (DZVP2).⁵⁹ Electronic exchange and correlation effects
578 were described within the generalized gradient approximation (GGA) in the
579 Perdew–Burke–Ernzerhof (PBE) parametrization.^{60,61} No symmetry constraints were
580 imposed. In deMon2k code, for all atoms, automatically generated auxiliary functions up to
581 orbital quantum number, $l = 3$ were used for fitting the density with the GGA functionals.⁶²
582 The GGA functionals were also coupled to an empirical dispersion (D) term.⁶³ A quasi-
583 Newton method in internal redundant coordinates with analytical energy gradients was used
584 for structure optimization of ferrous and ferric models in high spin state. For the numerical

585 integrations of the XC energy and potential, we used an adaptive grid with tighten threshold
586 (10^{-8} a.u.).⁶⁴ The convergence was based on the Cartesian gradient and displacement vectors
587 with thresholds of 10^{-3} a.u. and the energy convergence was set to 10^{-7} a.u. The DFT
588 calculations with periodic boundary conditions, carried out with VASP code, used the models
589 2e and 2a to build the unit cells for periodic calculations. In the case of the cluster model 1e,
590 the corresponding periodic structure 2e was modelled using a cell size $17.19 \text{ \AA} \times 20.89 \text{ \AA}$. In
591 the case of model 1a, the corresponding periodic structure 2a was constructed using cell size
592 of $9.94 \text{ \AA} \times 12.64 \text{ \AA}$. Vacuum region of 15 \AA was introduced in the z -direction in order to
593 eliminate interactions between the graphene sheet and its periodic images. All the DFT
594 calculations with periodic boundary conditions (PBC) were performed using PBE exchange-
595 correlation functional and VASP 5.2 recommended projector augmented-wave
596 pseudopotentials.^{65,66} For the calculation of structural and electronic properties, standard
597 PAW potentials supplied with VASP were used, with 4 valence electrons for C (2s2 2p2),
598 with 5 electrons for O (2s 2p3), 8 valence electrons for Fe (4s2 3d6), and 6 valence electrons
599 for O (2s 2p 4), respectively. Electric field gradients at the positions of the Fe nuclei were
600 calculated using the method reported in reference⁶⁷ as implemented in VASP. When
601 calculating electric field gradient, we have used the corresponding GW potentials, which give
602 a better description of high-energy unoccupied states. For GW Fe pseudopotential that treats
603 3s and 3p states as valence states was used. Cut-off energy for the plane wave basis set of 800
604 eV, break condition for electronic SC-loop of 10^{-6} eV and $8 \times 8 \times 1$ gamma centred mesh for
605 the model 2a, and $4 \times 4 \times 1$ mesh for the model 2e were found to lead to the converged electric
606 field gradients. In all cases, the Fermi-Dirac smearing method with sigma set to 0.03 was
607 used. In addition, all the calculations included support grid for the evaluation of the
608 augmentation charges.

609 The Bader charge density analysis⁶⁸ with the implementation of Henkelman and co-workers⁶⁹
610 in VASP code was used to obtain the spin charge density of the periodic structures. The
611 charge-spin density of the cluster structures was obtained using Mulliken population scheme.
612 The atomic spin densities were computed for all cluster and periodic models in order to verify
613 the spin density at the ferric or ferrous Fe site. The Fe spin density in its high and
614 intermediate spins was found to amount to $\sim 4e^-$ and $\sim 2e^-$, respectively. Note that in high-spin
615 models, spin-polarisation of C and N sites occurs prior to the increase of spin density on Fe.
616 Therefore, the total spin of each cluster or unit cell model was increased until the spin density
617 on Fe became $\sim 4e^-$, for which the quadrupole splitting energies were obtained (see
618 Supplementary **Table 5**). This approach differs from our previous study on high-spin ferric
619 models,³³ where the spin-state referred to the total spin of the clusters.

620 The quadrupole splitting energy is computed as the coupling between the nuclear quadrupole
621 moment (Q) the non-spherical nucleus and the principle components V_{ii} ($i=x,y,z$) of the
622 electric field gradient (EDF) tensor at ⁵⁷Fe nucleus using the following equation:

$$623 \quad \Delta E_Q = \frac{1}{2} eQV_{zz} \sqrt{1 + \frac{\eta^2}{3}} \quad (1)$$

624 Where e is the charge of the electron and the asymmetry parameter η is computed as =
625 $(V_{xx} - V_{yy})/V_{zz}$, where $|V_{zz}| \geq |V_{yy}| \geq |V_{xx}|$. The nuclear quadrupole moment, Q , for $J=3/2$
626 state is taken to be 0.16 barn. Computation of ΔE_Q and η therefore becomes a question of
627 computing the EFG tensor, which is readily obtained as an expectation value of the EFG
628 operator, $V_{ij} = \langle \Psi_0 \left| \frac{3ij-r^2}{r^5} \right| \Psi_0 \rangle$, for the electronic ground state Ψ_0 and $i,j=x,y,z$ being the
629 components of the electron radius vector r . For a direct comparison to experimentally
630 reported values, calculated values of ΔE_Q are reported in units of $\text{mm}\cdot\text{s}^{-1}$.

631

632

633 **Data availability**

634 The raw data that support the findings of this study are available from the
635 corresponding authors upon request. In particular: The X-ray absorption
636 spectroscopy raw data associated with this work is permanently stored at
637 synchrotron SOLEIL and available upon request; the raw data related to electron microscopy
638 images are permanently stored at LEPMI and available upon request; the raw data related to
639 X-ray radiographs are permanently stored at the APS synchrotron and available upon request;
640 the ⁵⁷Fe Mössbauer spectroscopy data and the raw and reconstructed tomography data are
641 available at Institut Charles Gerhardt Montpellier and available upon request.

642 **Code availability**

643 The source code used for DFT calculation with deMon2k is available at [http://www.demon-
644 software.com/public_html/download.html](http://www.demon-
644 software.com/public_html/download.html), upon request for academic purpose. The Vienna
645 Ab Initio Simulation Package (VASP) is a proprietary software available for purchase at
646 <https://www.vasp.at/>.

647

648 **References**

- 649 1. Katsounaros, I., Cherevko, S., Zeradjanin, A. R. & Mayrhofer, K. J. J. Oxygen
650 electrochemistry as a cornerstone for sustainable energy conversion. *Angew. Chem. Int. Ed.*
651 **53**, 102-121 (2014).
- 652 2. Chen, Y., Ji, S., Zhao, S., Chen, W., Dong, J., Cheong, W.-C., Shen, R., Wen, X., Zheng,
653 L., Rykov, A. I., Cai, S., Tang, H., Zhuang, Z., Chen, C., Peng Q., Wang, D. & Li, Y.
654 Enhanced oxygen reduction with single-atomic-site iron catalysts for a zinc-air battery and
655 hydrogen-air fuel cell. *Nat. Commun.* **9**, 5422 (2018).
- 656 3. Jung, H.-G., Hassoun, J., Park, J.-B., Sun, Y.-K. & Scrosati, B. An improved high-
657 performance lithium–air battery. *Nat. Chem.* **4**, 579-582 (2012).
- 658 4. Sharma, S. & Pollet, B. G. Support materials for PEMFC and DMFC electrocatalysts—a
659 review. *J. Power Sources* **208**, 96-119 (2012).
- 660 5. Rahimnejad, M., Adhami, A., Darvari, S., Zirepour, A. & Oh, S.-E. Microbial fuel cell as
661 new technology for bioelectricity generation: a review. *Alex. Eng. J.* **54**, 745-756 (2015).
- 662 6. Yin, X., Lin, L., Martinez, U. & Zelenay, P. 2, 2'-Dipyridylamine as Heterogeneous
663 organic molecular electrocatalyst for two-electron oxygen reduction reaction in acid media.
664 *ACS Appl. Energy Mater.* **2**, 7272-7278 (2019).
- 665 7. Sun, Y., Silvioli, L., Sahraie, N. R., Ju, W., Li, J., Zitolo, A., Li, S., Bagger, A., Arnarson,
666 L., Wang, X., Moeller, T., Bernsmeier, D., Rossmeisl, J., Jaouen, F. & Strasser, P. Activity–
667 selectivity trends in the electrochemical production of hydrogen peroxide over single-site
668 metal–nitrogen–carbon catalysts. *J. Am. Chem. Soc.* **141**, 12372-12381 (2019).
- 669 8. Yang, S., Verdager-Casadevall, A., Arnarson, L., Silvioli, L., Colic, V., Frydendal, R.,
670 Rossmeisl, J., Chorkendorff, I. & Stephens, I. E. L. Toward the decentralized electrochemical
671 production of H₂O₂: a focus on the catalysis. *ACS Catal.* **8**, 4064-4081 (2018).
- 672 9. Moussallem, I., Pinnow, S., Wagner, N. & Turek, T. Development of high-performance
673 silver-based gas-diffusion electrodes for chlor-alkali electrolysis with oxygen depolarized
674 cathodes. *Chem. Eng. Process.* **52**, 125-131 (2012).
- 675 10. Ziegelbauer, J. M., Gullá, A. F., O'Laoire C., Urgeghe, C., Allen, R. J. & Mukerjee, S.
676 Chalcogenide electrocatalysts for oxygen-depolarized aqueous hydrochloric acid electrolysis.
677 *Electrochim. Acta* **52**, 6282-6294 (2007).
- 678 11. Li, J., Jia, Q., Ghoshal, S., Liang, W. & Mukerjee, S. Highly active and stable Fe-N-C
679 catalyst for oxygen depolarized cathode applications. *Langmuir* **33**, 9246-9253 (2017).
- 680 12. Wang, X. X., Swihart, M. T. & Wu, G. Achievements, challenges and perspectives on
681 cathode catalysts in proton exchange membrane fuel cells for transportation. *Nat. Catal.* **2**,
682 578-589 (2019).
- 683 13. Ott, S., Orfanidi, A., Schmies, H., Anke, B., Nong H. N., Hübner, J., Gernert, U., Glied,
684 M., Lerch, M. & Strasser P. Ionomer distribution control in porous carbon-supported catalyst
685 layers for high-power and low Pt-loaded proton exchange membrane fuel cells. *Nat. Mater.*
686 **19**, 77-85 (2019).
- 687 14. Huang, X., Zhao, Z., Cao, L., Chen, Y., Zhu, E., Lin, Z., Li, M., Yan, A., Zettl, A., Wang,
688 Y. M., Duan, X., Mueller, T. & Huang, Y. High-performance transition metal–doped Pt₃Ni
689 octahedra for oxygen reduction reaction. *Science* **348**, 1230-1234 (2015).
- 690 15. Zitolo, A., Goellner, V., Armel, V., Sougrati, M.-T., Mineva, T., Stievano, L., Fonda, E.
691 & Jaouen, F. Identification of catalytic sites for oxygen reduction in iron-and nitrogen-doped
692 graphene materials. *Nat. Mater.* **14**, 937-942 (2015).
- 693 16. Zitolo, A., Ranjbar-Sahraie, N., Mineva, T., Li, J., Jia, Q., Stamatini, S., Harrington, G. F.,
694 Lyth, S. M., Krtil, P., Mukerjee, S., Fonda, E. & Jaouen, F. Identification of catalytic sites in
695 cobalt-nitrogen-carbon materials for the oxygen reduction reaction. *Nat. Commun.* **8**, 957
696 (2017).

697 17. Proietti, E., Jaouen, F., Lefèvre, M., Larouche, N., Tian, Juan, Herranz, J. & Dodelet, J.-P.
698 Iron-based cathode catalyst with enhanced power density in polymer electrolyte membrane
699 fuel cells. *Nat. Commun.* **2**, 416 (2011).

700 18. Chung, H. T., Cullen, D. A., Higgins, D., Sneed, B. T., Holby, E. F., More, K. L.,
701 Zelenay, P. Direct atomic-level insight into the active sites of a high-performance PGM-free
702 ORR catalyst. *Science* **357**, 479-484 (2017).

703 19. Choi, C. H., Baldizzone, C., Polymeros, G., Pizzutilo, E., Kasian, O., Schuppert, A. K.,
704 Sahraie, N. R., Sougrati, M.-T., Mayrhofer, K. J. J. & Jaouen, F. Minimizing operando
705 demetallation of Fe-NC electrocatalysts in acidic medium. *ACS Catal.* **6**, 3136-3146 (2016).

706 20. Choi, C. H., Choi, W. S., Kasian, O., Mechler, A. K., Sougrati, M. T., Brüller, S.,
707 Strickland, K., Jia, Q., Mukerjee, S., Mayrhofer, K. J. J. & Jaouen, F. Unraveling the nature
708 of sites active toward hydrogen peroxide reduction in Fe-N-C catalysts. *Angew. Chem. Int.*
709 *Ed.* **56**, 8809-8812 (2017).

710 21. Kumar, K., Gairola, P., Ranjbar-Sahraie, N., Mermoux, M., Duban, L., Zitolo, A., Jaouen,
711 F. & Maillard, F. Physical and chemical considerations for improving catalytic activity and
712 stability of non-precious-metal oxygen reduction reaction catalysts. *ACS Catal.* **8**, 11264-
713 11276 (2018).

714 22. Chenitz, R., Kramm, U. I., Lefèvre M., Glibin, V., Zhang, G., Sun, S. & Dodelet, J.-P. A
715 specific demetalation of Fe-N₄ catalytic sites in the micropores of NC_Ar + NH₃ is at the
716 origin of the initial activity loss of the highly active Fe/N/C catalyst used for the reduction of
717 oxygen in PEM fuel cells. *Energy Environ. Sci.* **11**, 365-382 (2018).

718 23. Ferrandon, M., Wang, X., Kropf, A. J., Myers, D. J., Wu, G., Johnston, C. M. & Zelenay,
719 P. Stability of iron species in heat-treated polyaniline-iron-carbon polymer electrolyte fuel
720 cell cathode catalysts. *Electrochim. Acta* **110**, 282-29 (2013).

721 24. Lefèvre, M. & Dodelet, J.-P. Fe-based catalysts for the reduction of oxygen in polymer
722 electrolyte membrane fuel cell conditions: determination of the amount of peroxide released
723 during electroreduction and its influence on the stability of the catalysts. *Electrochim. Acta*
724 **48**, 2749-2760 (2003).

725 25. Choi, C. H., Lim, H.-K., Chung, M. W., Chon, G., Sahraie, N. R., Altin, A., Sougrati, M.-
726 T., Stievano, L., Oh, H. S., Park, E. S., Luo, F., Strasser, P., Dražić, G., Mayrhofer, K. J. J.,
727 Kim, H. & Jaouen, F. The achilles' heel of iron-based catalysts during oxygen reduction in an
728 acidic medium. *Energy Environ. Sci.* **11**, 3176-3182 (2018).

729 26. Choi, C. H., Baldizzone, C., Grote, J.-P., Schuppert, A. K., Jaouen, F. & Mayrhofer, K. J.
730 J. Stability of Fe-N-C catalysts in acidic medium studied by operando spectroscopy. *Angew.*
731 *Chem. Int. Ed.* **54**, 12753-12757 (2015).

732 27. Goellner, V., Baldizzone, C., Schuppert, A., Sougrati, M. T., Mayrhofer, K. & Jaouen, F.
733 Degradation of Fe/N/C catalysts upon high polarization in acid medium. *Phys. Chem. Chem.*
734 *Phys.* **16**, 18454-18462 (2014).

735 28. Herranz, J., Jaouen, F., Lefèvre, M., Kramm, U. I., Proietti, E., Dodelet, J.-P., Bogdanoff,
736 P., Fiechter, S., Abs-Wurmbach, I., Bertrand, P., Arruda, T. M. & Mukerjee, S. Unveiling N-
737 protonation and anion-binding effects on Fe/N/C catalysts for O₂ reduction in proton-
738 exchange-membrane fuel cells. *J. Phys. Chem. C* **115**, 16087-16097 (2011).

739 29. Santori, P. G., Speck, F. D., Li, J., Zitolo, A., Jia, Q., Mukerjee, S., Cherevko, S. &
740 Jaouen, F. Effect of Pyrolysis Atmosphere and electrolyte pH on the oxygen reduction
741 activity, stability and spectroscopic signature of FeN_x moieties in Fe-N-C catalysts. *J.*
742 *Electrochem. Soc.* **166**, F3311-F3320 (2019).

743 30. Kumar, K., Dubau, L., Mermoux, M., Li, J., Zitolo, A., Nelayah, J., Jaouen, F. & Maillard,
744 F. On the influence of oxygen on the degradation of Fe-N-C catalysts. *Angew. Chem. Int. Ed.*
745 **59**, 3235-3243 (2020).

- 746 31. Kramm, U. I., Herranz, J., Larouche, N., Arruda, T., Lefèvre, M., Jaouen, F., Bogdanoff,
747 P., Fiechter, S., Abs-Wurmbach, I., Mukerjee, S. & Dodelet, J.-P. Structure of the catalytic
748 sites in Fe/N/C-catalysts for O₂-reduction in PEM fuel cells. *Phys. Chem. Chem. Phys.* **14**,
749 11673-11688 (2012).
- 750 32. Kramm, U. I., Lefèvre, M., Larouche, N., Schmeisser, D. & Dodelet, J.-P. Correlations
751 between mass activity and physicochemical properties of Fe/N/C catalysts for the ORR in
752 PEM fuel cell via ⁵⁷Fe Mossbauer spectroscopy and other techniques. *J. Am. Chem. Soc.* **136**,
753 978-985 (2014).
- 754 33. Mineva, T., Matanovic, I., Atanassov, P., Sougrati, M.-T., Stievano, L., Clémancey, M.,
755 Kochem, A., Latour, J.-M. & Jaouen F. Understanding active sites in pyrolyzed Fe-N-C
756 catalysts for fuel cell cathodes by bridging density functional theory calculations and ⁵⁷Fe
757 Mössbauer Spectroscopy. *ACS Catal.* **9**, 9359-9371 (2019).
- 758 34. Wagner, S., Auerbach, H., Tait, C. E., Martinaiou, I., Kumar, S. C. N., Kübel, C., Sergeev,
759 I., Wille, H.-C., Behrends, J., Wolny, J. A., Schünemann, V., Kramm, U. I. Elucidating the
760 structural composition of a Fe-N-C catalyst by nuclear and electron resonance techniques.
761 *Angew. Chem. Int. Ed.* **58**, 10486-10492 (2019).
- 762 35. Zelenay, P. & Myers, D. J. Hydrogen and Fuel Cells Program-2019 Annual Merit Review
763 and Peer Evaluation Meeting- ElectroCat (Electrocatalysis Consortium).
764 https://www.hydrogen.energy.gov/pdfs/review19/fc160_myers_zelenay_2019_o.pdf
- 765 36. Banham, D., Kishimoto, T., Zhou, Y., Sato, T., Bai, K., Ozaki, J-i, Imashiro, Y. & Ye, S.
766 Critical advancements in achieving high power and stable nonprecious metal catalyst-based
767 MEAs for real-world proton exchange membrane fuel cell applications. *Sci. Adv.* **4**, 7180
768 (2018).
- 769 37. Zboril, R., Mashlan, M. & Petridis, D. Iron(III) oxides from thermal processes - synthesis,
770 structural and magnetic properties, Mössbauer spectroscopy characterization, and
771 applications. *Chem. Mater.* **14**, 969-982 (2002).
- 772 38. Kamali-M, S., Ericsson, T. & Wäppling, R. Characterization of iron oxide nanoparticles
773 by Mössbauer spectroscopy. *Thin Solid Films* **515**, 721-723 (2006).
- 774 39. Lyubutin, I. S., Starchikov, S. S., Lin, C.-R., Gervits, N. E., Korotkov, N. Y. & Bukreeva,
775 T. V. Structural and magnetic properties of iron oxide nanoparticles in shells of hollow
776 microcapsules designed for biomedical applications. *Croat. Chem. Acta* **88**, 397-403 (2015).
- 777 40. Sougrati, M. T., Goellner, V., Schuppert, A. K., Stievano, L. & Jaouen, F. Probing active
778 sites in iron-based catalysts for oxygen electro-reduction: A temperature-dependent ⁵⁷Fe
779 Mössbauer spectroscopy study. *Catal. Today* **262**, 110-120 (2016).
- 780 41. Principi, E., Di Cicco, A., Witkowska, A. & Marassi, R. Performance of a fuel cell
781 optimized for *in situ* X-ray absorption experiments. *J. Synchrotron Rad.* **14**, 276-281 (2007).
- 782 42. Li, J., Ghoshal, S., Liang, W., Sougrati, M.-T., Jaouen, F., Halevi, B., Mckinney, S.,
783 McCool, G., Ma, C., Yuan, X., Ma, Z.-F., Mukerjee, S. & Jia, Q. Structural and mechanistic
784 basis for the high activity of Fe-N-C catalysts toward oxygen reduction. *Energy Environ. Sci.*
785 **9**, 2418-2432 (2016).
- 786 43. Osmieri, L., Ahluwalia, R. K., Wang, X., Chung, H. T., Yin, X., Kropf, A. J., Park, J.,
787 Cullen, D. A., More, K. L., Zelenary, P., Myers, D. J. & Neyerlin, K. C. Elucidation of Fe-N-
788 C electrocatalyst active site functionality via in-situ X-ray absorption and operando
789 determination of oxygen reduction reaction kinetics in a PEFC. *Appl. Catal. B* **257**, 117929
790 (2019).
- 791 44. Li, J., Alsudairi, A., Ma, Z.-F., Mukerjee, S. & Jia, Q. Asymmetric volcano trend in
792 oxygen reduction activity of Pt and non-Pt catalysts: in situ identification of the site-blocking
793 effect. *J. Am. Chem. Soc.* **139**, 1384-1387 (2017).
- 794 45. Fultz, B. "Mössbauer spectrometry." *Characterization of materials* 1-21 (2002).

795 46. Bonomi, F., Ichiye, T., Hendrich, M., Lindahl, P., Chakrabarti, M., Ribbe, M., Hu, Y.,
796 Einsle, O., Jarrett, J., Hille, R. & Booker, S. Characterization, Properties and Applications.
797 Walter de Gruyter GmbH & Co KG. (2017).

798 47. Vankó, G., Neisius, T., Molnár, G., Renz, F., Kárpárti, S., Shukla, A & de Groot, F. M. F.
799 Probing the 3d spin momentum with X-ray emission spectroscopy: The case of molecular-
800 spin transitions. *J. Phys. Chem. B* **110**, 11647-11653 (2006).

801 48. Jia, Q., Ramaswamy, N., Hafiz, H., Tylus, U., Strickland, K., Wu, G., Barbiellini, B.,
802 Bansil, A., Holby, E. F., Zelenary, P. & Mukerjee, S. Experimental observation of redox-
803 induced Fe–N switching behavior as a determinant role for oxygen reduction activity. *ACS*
804 *Nano* **9**, 12496-12505 (2015).

805 49. Hossen, M. M., Artyushkova, K., Atanassov, P. & Serov, A. Synthesis and
806 characterization of high performing Fe-N-C catalyst for oxygen reduction reaction (ORR) in
807 alkaline exchange membrane fuel cells. *J. Power Sources* **375**, 214-221 (2018).

808 50. Varela, A. S., Kroschel, M., Leonard, N. D., Ju, W., Steinberg, J., Bagger, A., Rossmeisl,
809 J. & Strasser, P. pH Effects on the Selectivity of the Electrocatalytic CO₂ Reduction on
810 Graphene-Embedded Fe–N–C Motifs: Bridging Concepts between Molecular Homogeneous
811 and Solid-State Heterogeneous Catalysis. *ACS Energy Lett.* **3**, 812-817 (2018).

812 51. Ablett, J. M., Prieur, D., Céolin, D., Lassalle-Kaiser, B., Lebert, B., Sauvage, M., Moreno,
813 T., Bac, S., Balédent, V., Ovono, A., Morand, M., Gélebart, F., Shukla, A. & Rueff, J. P. The
814 GALAXIES inelastic hard X-ray scattering end-station at Synchrotron SOLEIL. *J.*
815 *Synchrotron Radiat.* **26**, 263-271 (2019).

816 52. Rueff, J. P., Ablett, J. M., Céolin, D., Prieur, D., Moreno, T., Balédent, V., Lassalle-
817 Kaiser, B., Rault, J. E., Simon, M. & Shukla, A. The GALAXIES beamline at the SOLEIL
818 synchrotron: inelastic X-ray scattering and photoelectron spectroscopy in the hard X-ray
819 range. *J. Synchrotron Radiat.* **22**, 175-179 (2015).

820 53. Gürsoy, D., DeCarlo, F., Xiao X. & Jacobsen C. Tomopy: a framework for the analysis of
821 synchrotron tomographic data. *J. Synchrotron Radiat.*, **21**, 1188-1193 (2014).

822 54. Dragonfly 4.1 [Computer software]. Object Research Systems (ORS) Inc, Montreal,
823 Canada, 2019; software available at <http://www.theobjects.com/dragonfly>.

824 55. de la Lande, A., Alvarez-Ibarra, A., Hasnaoui, K., Cailliez, F., Wu, X., Mineva, T., Cuny,
825 J., Calaminici, P., López-Sosa, L., Geudtner, G., Navizet, I., Iriepa, C. G., Salahub, D. R.D.
826 & Köster, A. M. Molecular Simulations with in-deMon2k QM/MM, a Tutorial-Review.
827 *Molecules* **24**, 1653 (2019).

828 56. Koster, A. M. *et al. deMon2k*, Version 6, The deMon developers, Cinvestav, Mexico City
829 (2018).

830 57. Kresse, G. & Furthmüller, J. Efficient iterative schemes for ab initio total-energy
831 calculations using a plane-wave basis set. *Phys. Rev. B* **54**, 11169–11186 (1996).

832 58. Kresse, G. & Furthmüller, J. Efficiency of ab-initio total energy calculations for metals
833 and semiconductors using a plane-wave basis set. *Comput. Mater. Sci.* **6**, 15–50 (1996).

834 59. Godbout, N., Salahub, D. R., Andzelm, J. & Wimmer, E. Optimization of Gaussian-type
835 basis sets for local spin density functional calculations. Part I. Boron through neon,
836 optimization technique and validation. *CJC Univ. Calg. 50th Anniv. Virtual Issue* **01**, 560–
837 571 (2011).

838 60. Perdew, J. P., Burke, K. & Ernzerhof, M. Generalized Gradient Approximation Made
839 Simple. *Phys. Rev. Lett.* **77**, 3865–3868 (1996).

840 61. Zhang, Y. & Yang, W. Comment on "Generalized Gradient Approximation Made
841 Simple". *Phys. Rev. Lett.* **80**, 890–890 (1998).

842 62. Köster, A. M., Reveles, J. U. & Del, J. C. Calculation of exchange-correlation potentials
843 with auxiliary function densities. *J. Chem. Phys.* **121**, 3417–3424 (2004).

- 844 63. Wu, Q. & Yang, W. Empirical correction to density functional theory for van der Waals
845 interactions. *J. Chem. Phys.* **116**, 515–524 (2001).
- 846 64. Krack, M. & Köster, A. M. An adaptive numerical integrator for molecular integrals. *J.*
847 *Chem. Phys.* **108**, 3226–3234 (1998).
- 848 65. Blöchl, P. E. Projector augmented-wave method. *Phys. Rev. B* **50**, 17953–17979 (1994).
- 849 66. Kresse, G. & Joubert, D. From ultrasoft pseudopotentials to the projector augmented-
850 wave method. *Phys. Rev. B* **59**, 1758–1775 (1999).
- 851 67. Petrilli, H. M., Blöchl, P. E., Blaha, P. & Schwarz, K. Electric-field-gradient calculations
852 using the projector augmented wave method. *Phys. Rev. B* **57**, 14690-14697 (1998).
- 853 68. Bader, R. F. W. *Atoms in Molecules: A Quantum Theory*. Oxford University Press. (1994).
- 854 69. Tang, W., Sanville, E. & Henkelman, G. A grid-based Bader analysis algorithm without
855 lattice bias. *J. Phys. Condens. Matter* **21**, 084204 (2009).
- 856
857
858
859
860

861 **Acknowledgements**

862 The research leading to these results has received partial funding from
863 the French National Research Agency under the CAT2CAT contract
864 (ANR-16-CE05-0007), the FCH Joint Undertaking (CRESCENDO Project, Grant Agreement
865 n°779366) and the Centre of Excellence of Multifunctional Architected Materials
866 “CEMAM” (ANR-10-LABX-44-01) . We acknowledge Synchrotron SOLEIL (Gif-sur
867 Yvette, France) for provision of synchrotron radiation facilities at beamline GALAXIES
868 (proposal number 20170390) and at beamline SAMBA (proposal number 99190122). I.Z.
869 acknowledges the resources of the Advanced Photon Source, a U.S. Department of Energy
870 (DOE) Office of Science User Facility operated for the U.S. DOE Office of Science by
871 Argonne National Laboratory under contract No. DE-AC02-06CH11357. I. M. thankfully
872 acknowledges the computational resources of the National Energy Research Scientific
873 Computing Center (NERSC), a U.S. Department of Energy Office of Science User Facility
874 operated under Contract No. DE-AC02-05CH11231. This paper has been assigned LA-UR-
875 19-31453. The computational work of T.M and I.C.O. was granted access to the HPC
876 resources of IDRIS/TGCC under the allocation 2019 - A0050807369 made by GENCI and
877 supported by the LabExCheMISyst ANR-10-LABX-05-01. G. D. acknowledges the financial
878 support from Slovenian Research Agency (P2-0393).

879 **Author contributions**

880 J.L. and F.J. designed and synthesized the materials, and conducted the electrochemical and
881 physical characterizations. M.T.S. and J.L. designed and conducted the *in situ* and *ex situ*
882 Mössbauer spectroscopy measurements. M.T.S. conducted Mössbauer data analysis. A.Z. and
883 J.L. conducted the *operando* and *ex situ* XAS measurements. A.D.C. designed the *operando*
884 fuel cell for XAS. F.J., A.Z., J.L. and J.M.A. conducted the *in situ* XES experiments. I.C.O.,
885 T.M., I.M. and P.A. conducted the DFT computation. K.K., L.D. and F.M. performed TEM

886 and STEM-EDX analyses, G.D. performed atomic-scale STEM analyses, I.Z. and Y.H.
887 performed tomography and TEM analyses. J.L., M.T.S. and F.J. wrote and edited the
888 manuscript with input from all authors. The project was supervised by F.J.

889 **Additional information**

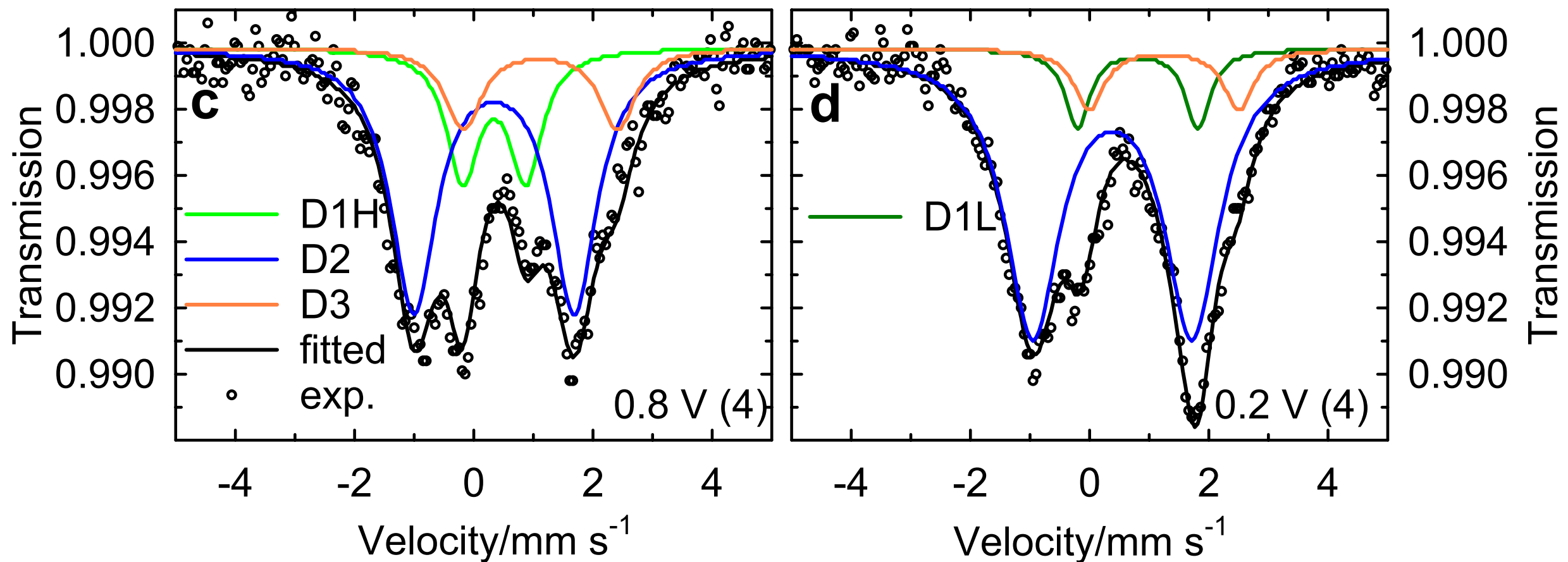
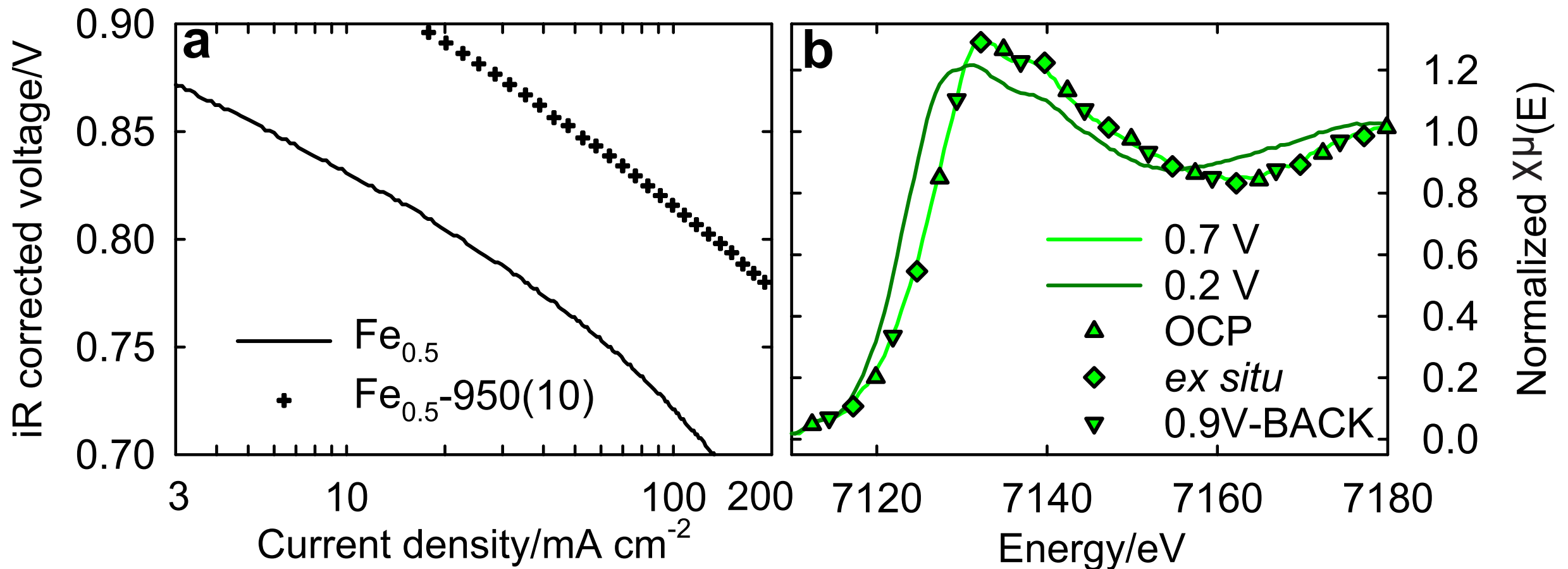
890 Supplementary information is available in the online version of the paper. Correspondence
891 and requests for materials should be addressed to F.J.

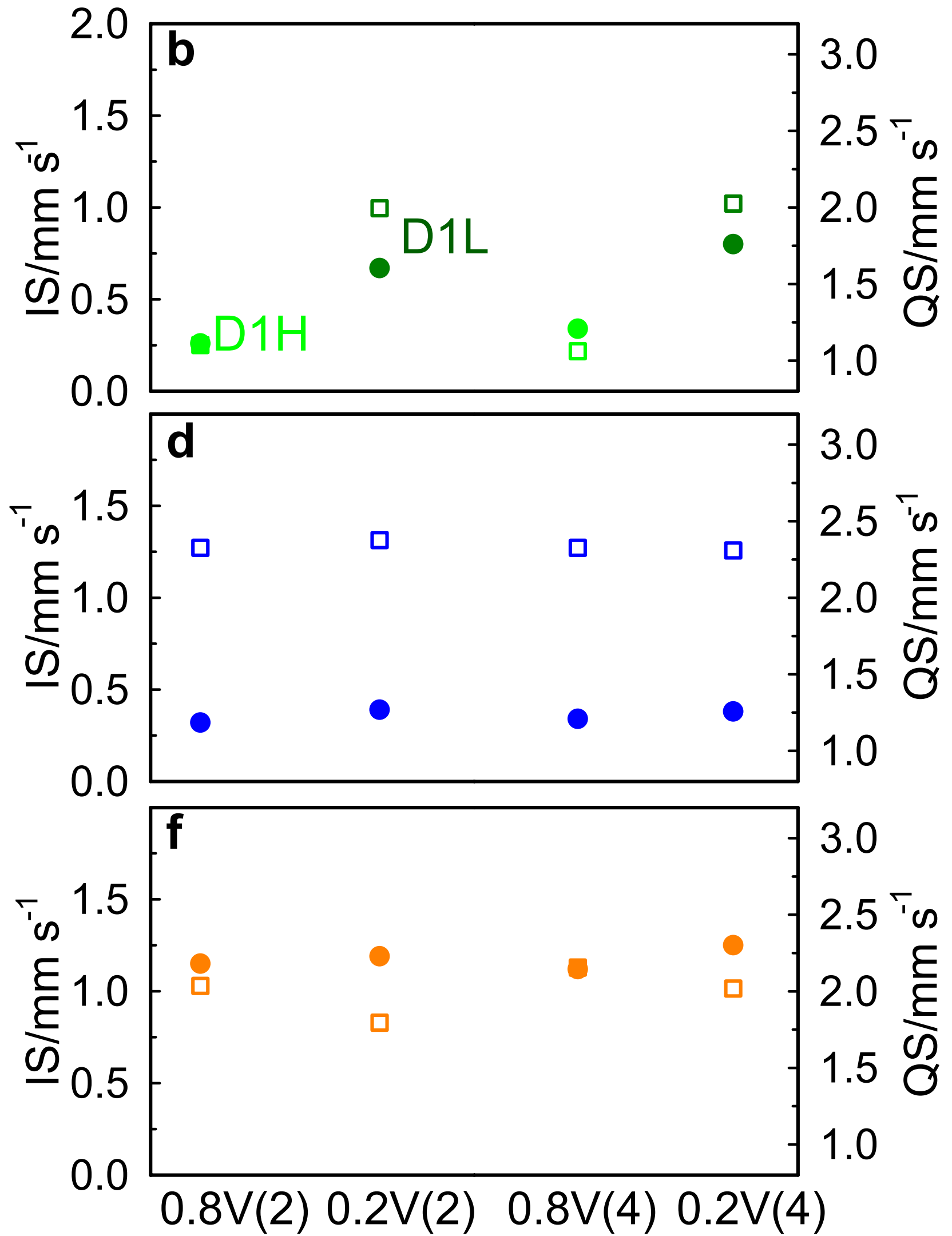
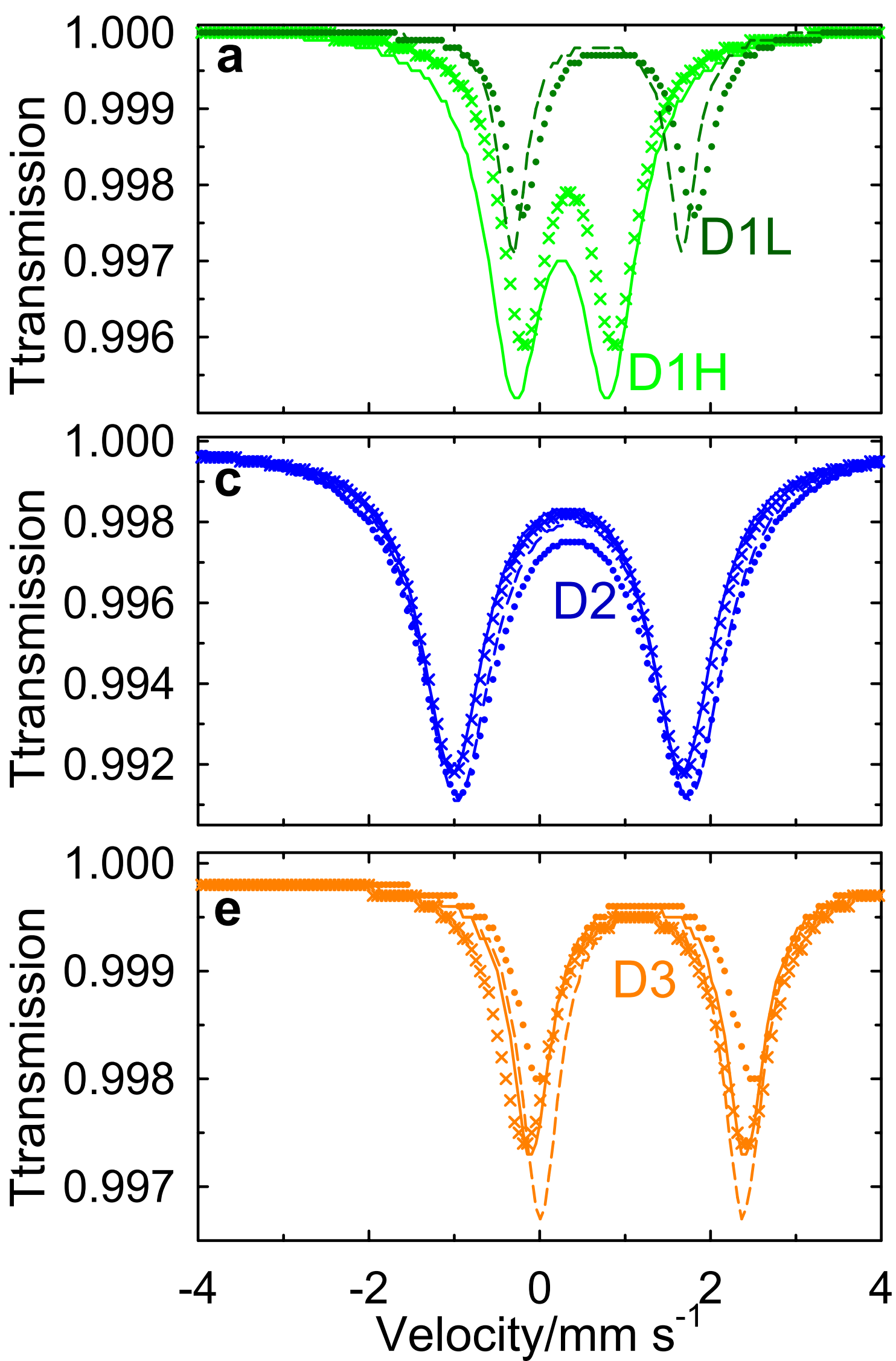
892 **Competing interests**

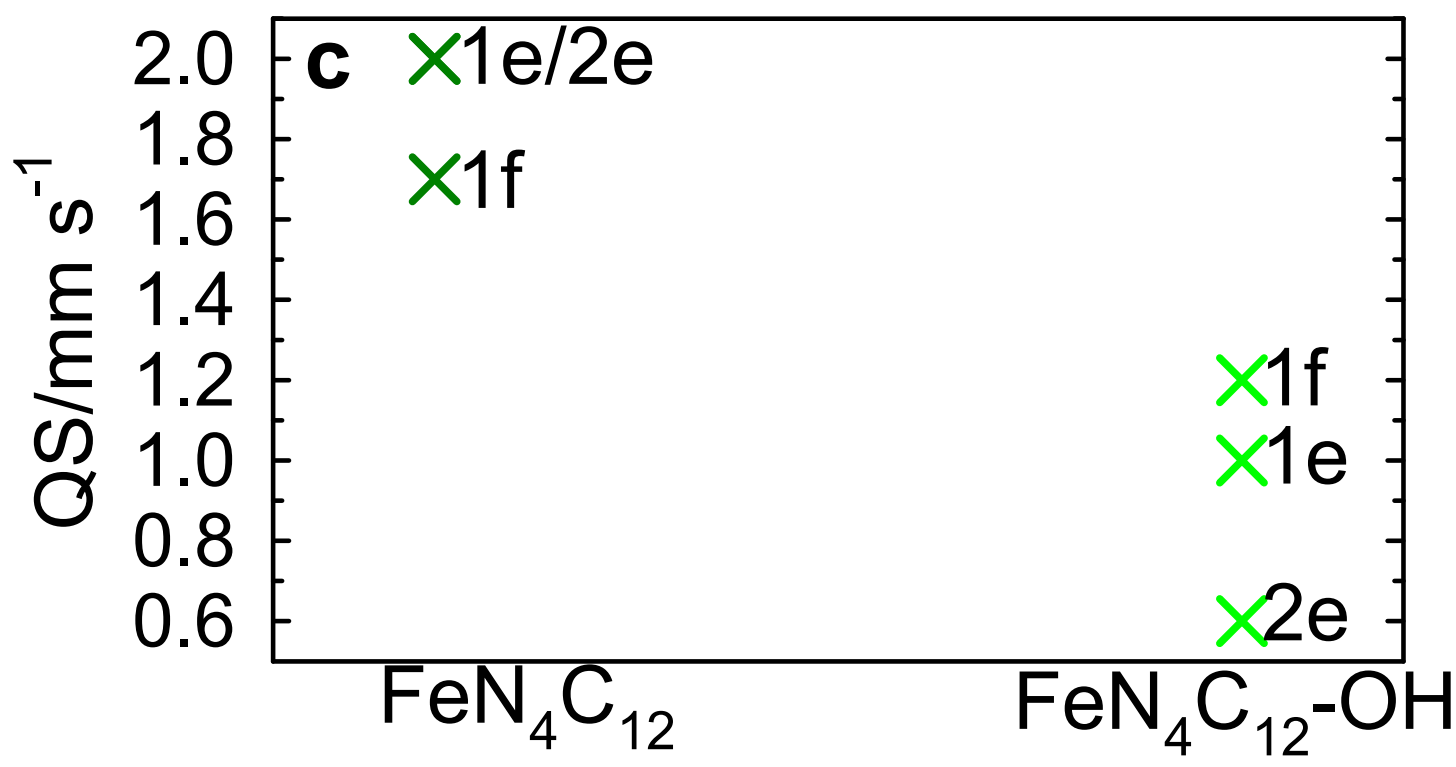
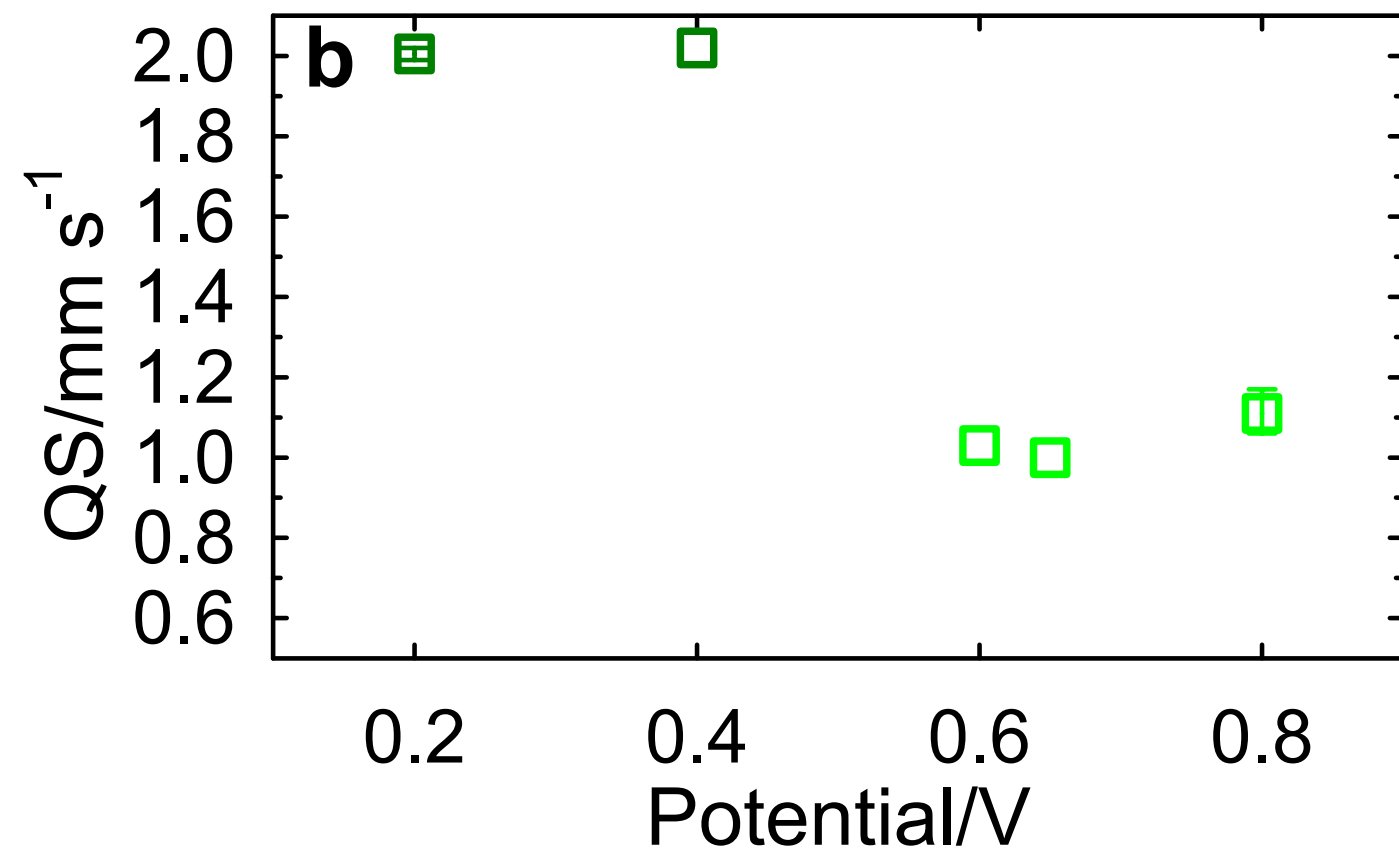
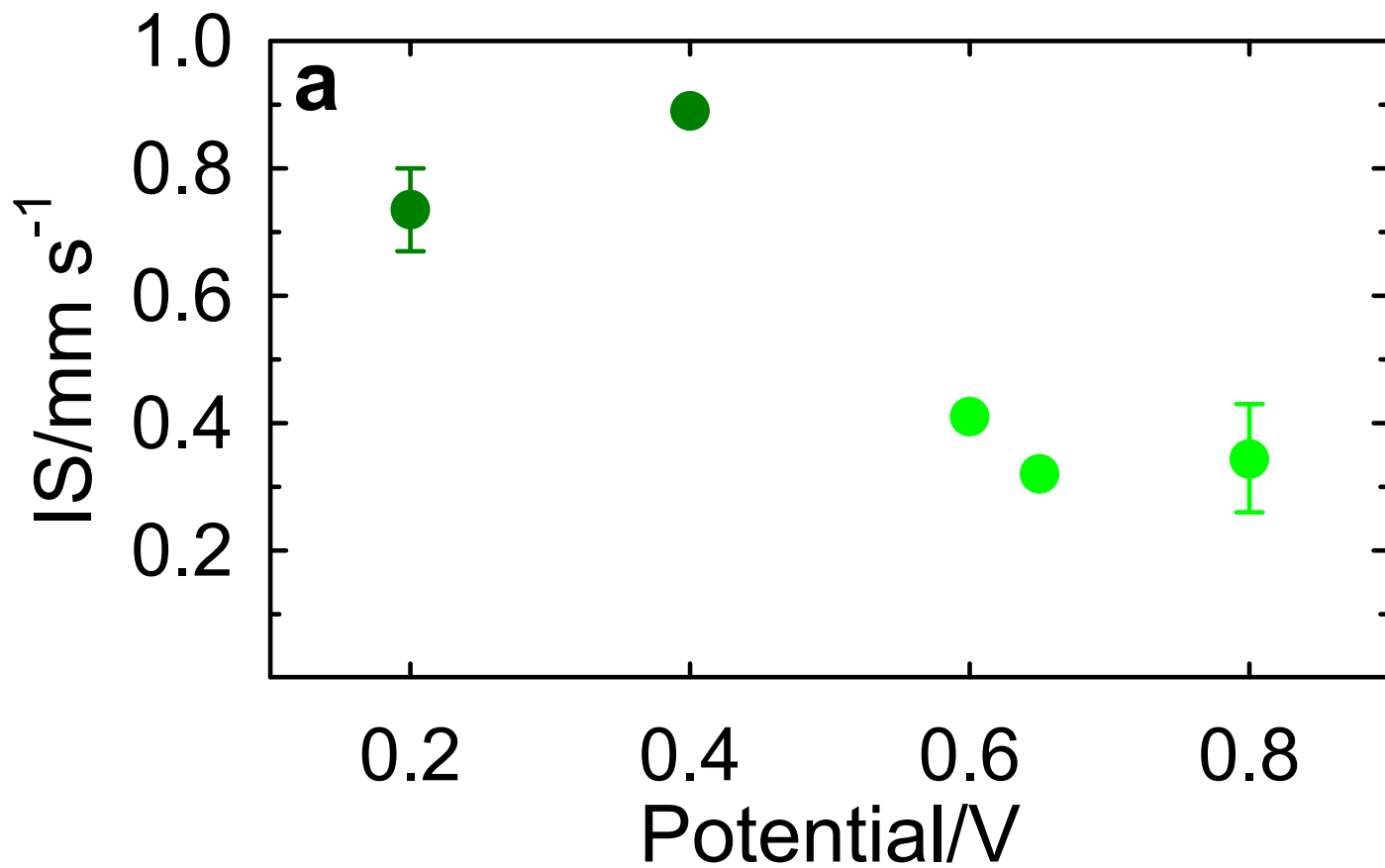
893 The authors declare no competing interests.

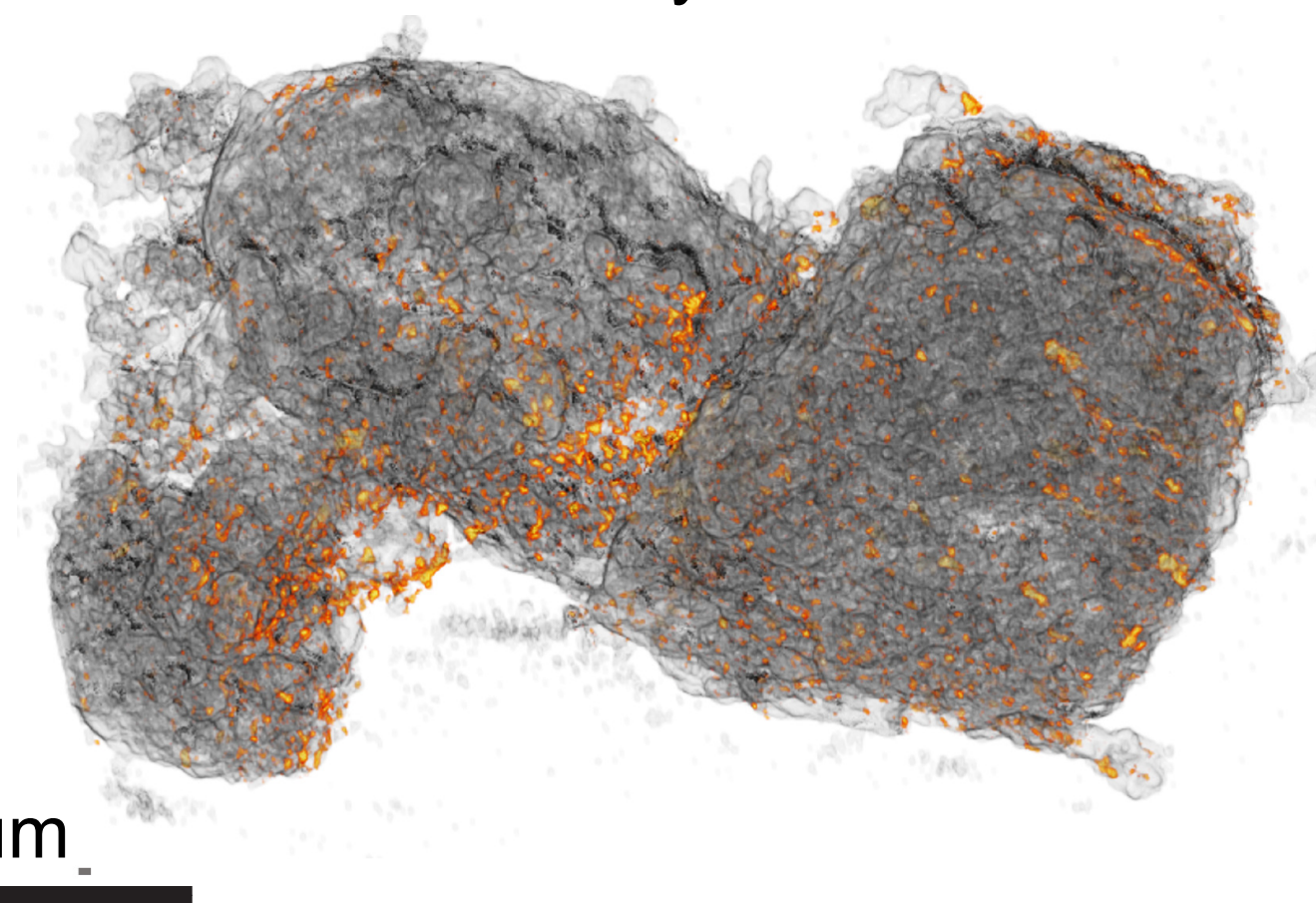
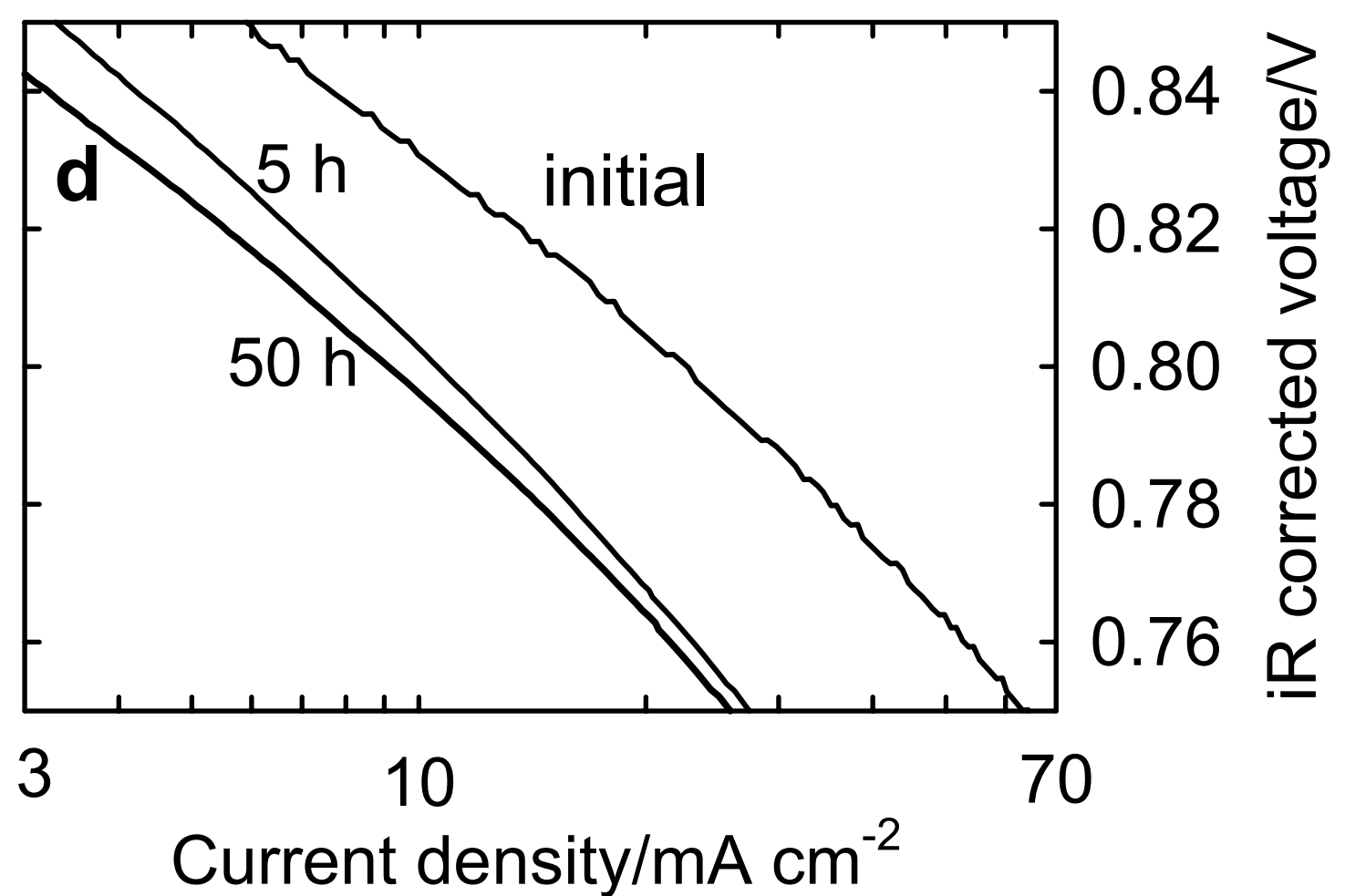
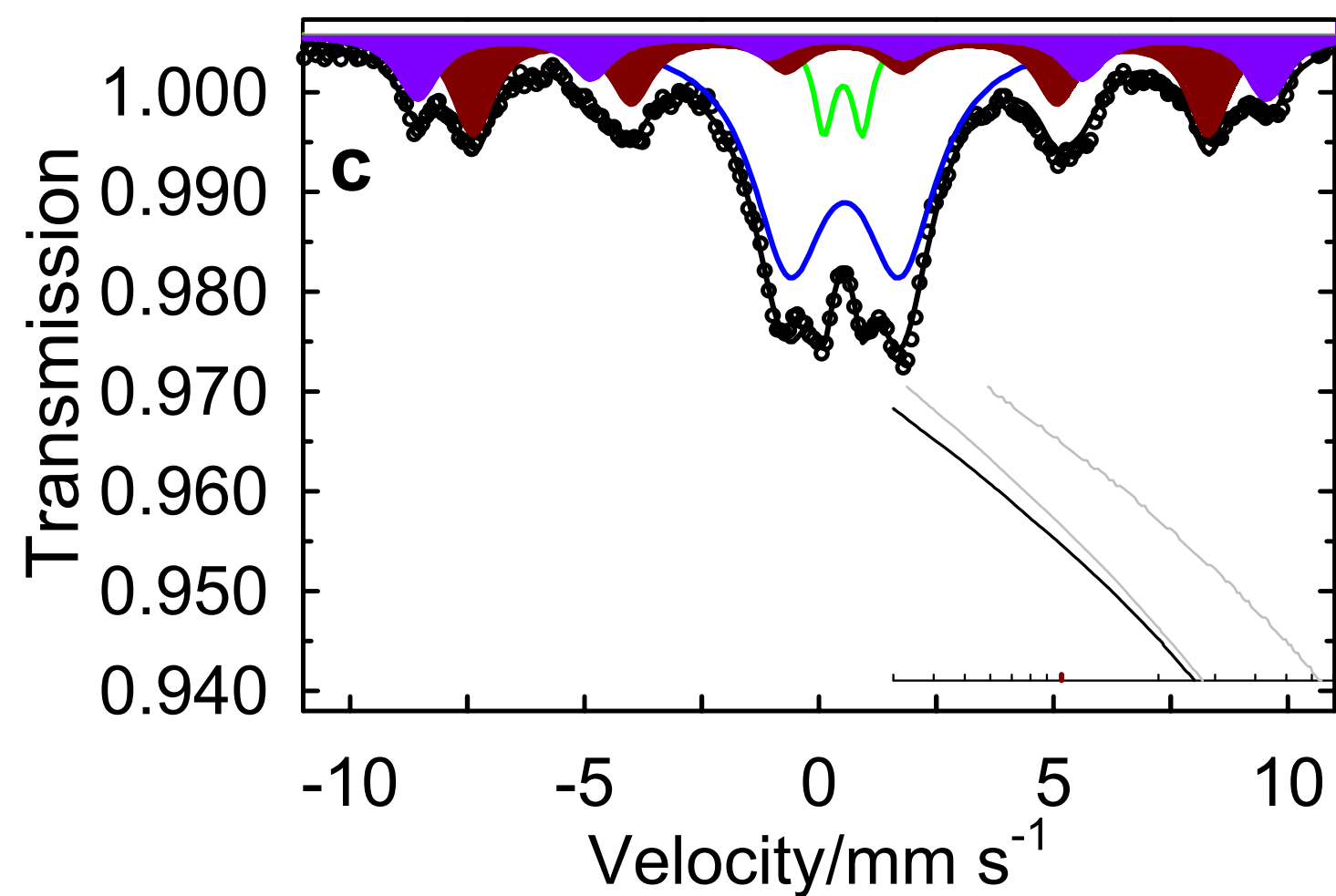
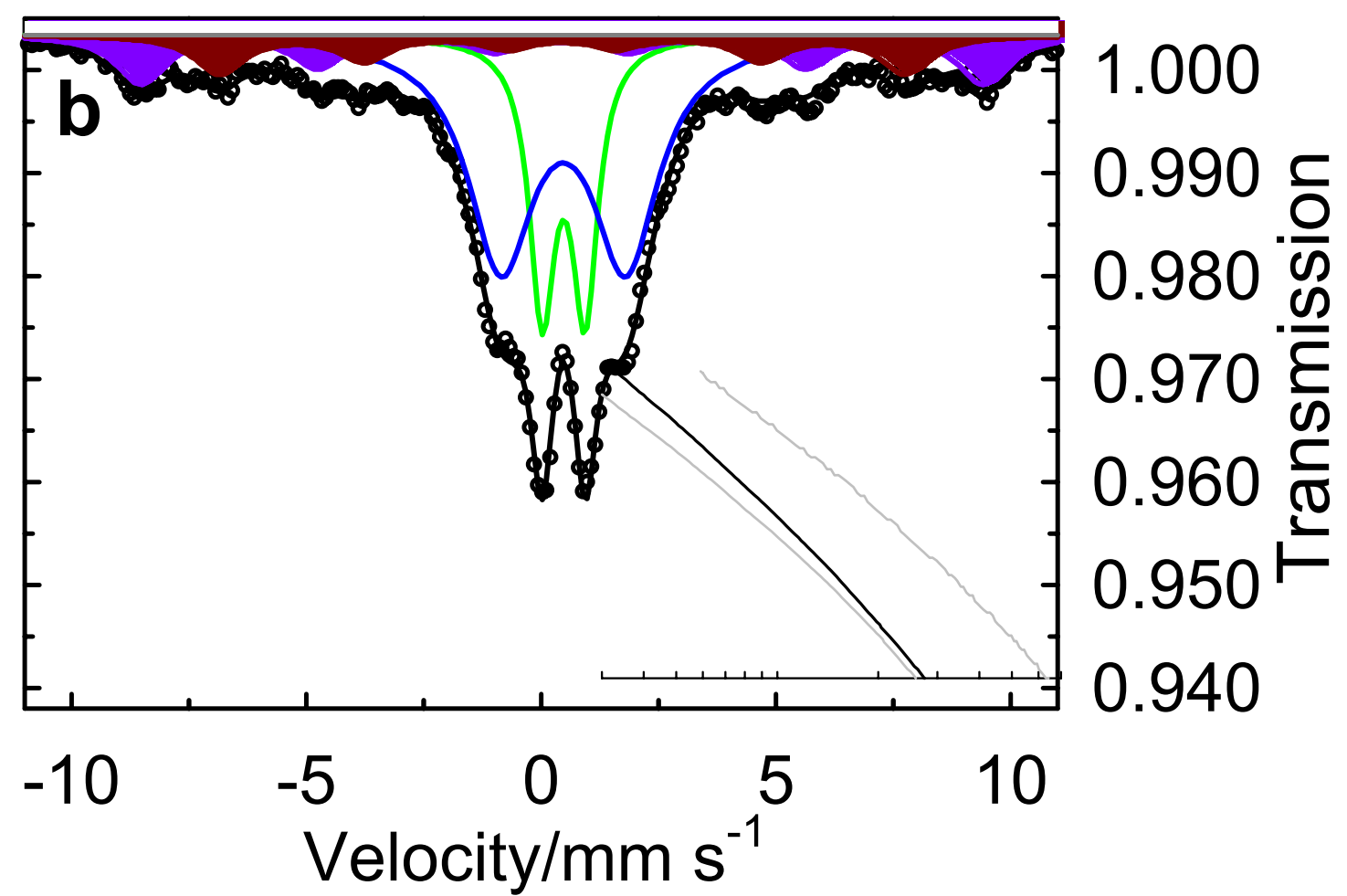
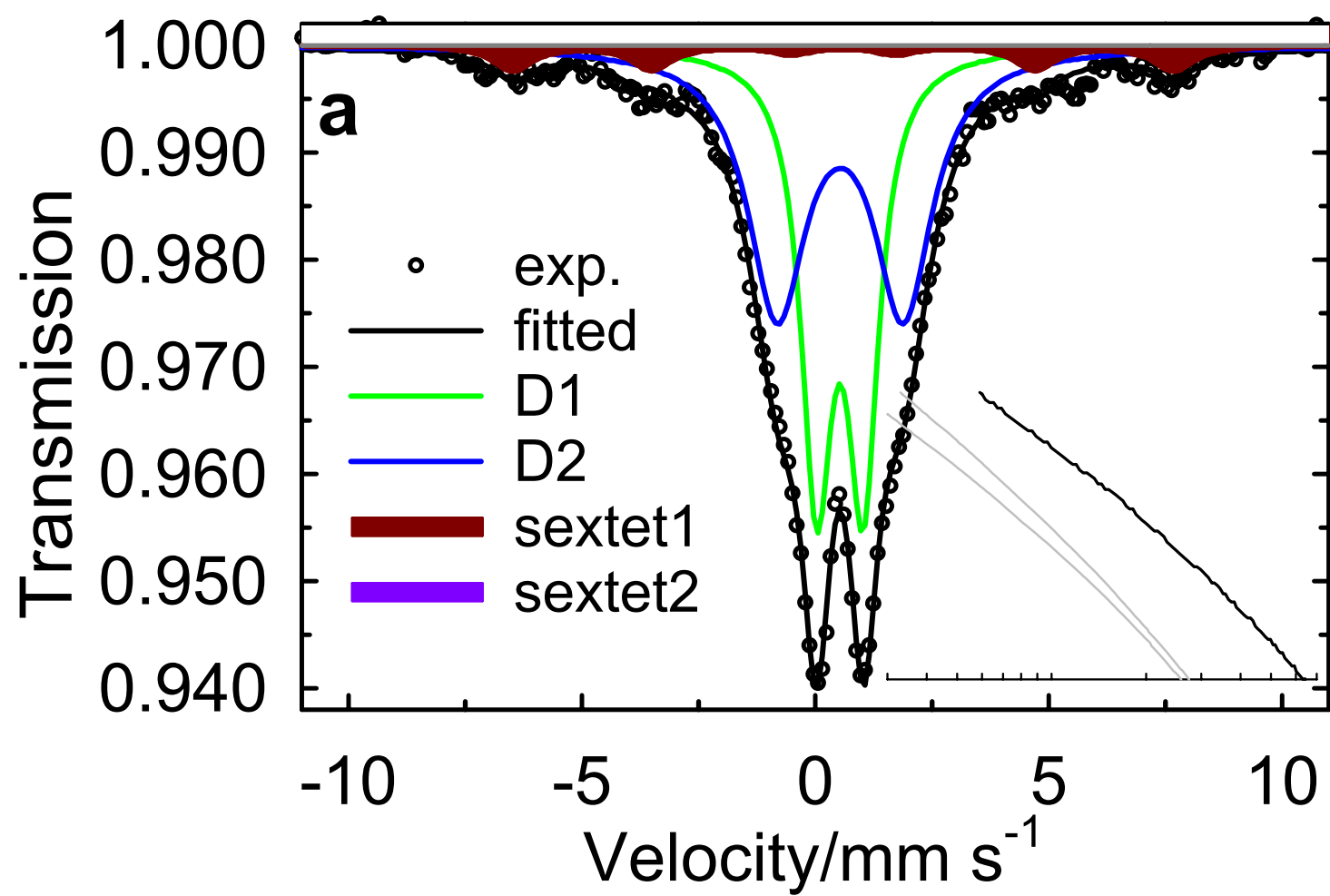
894

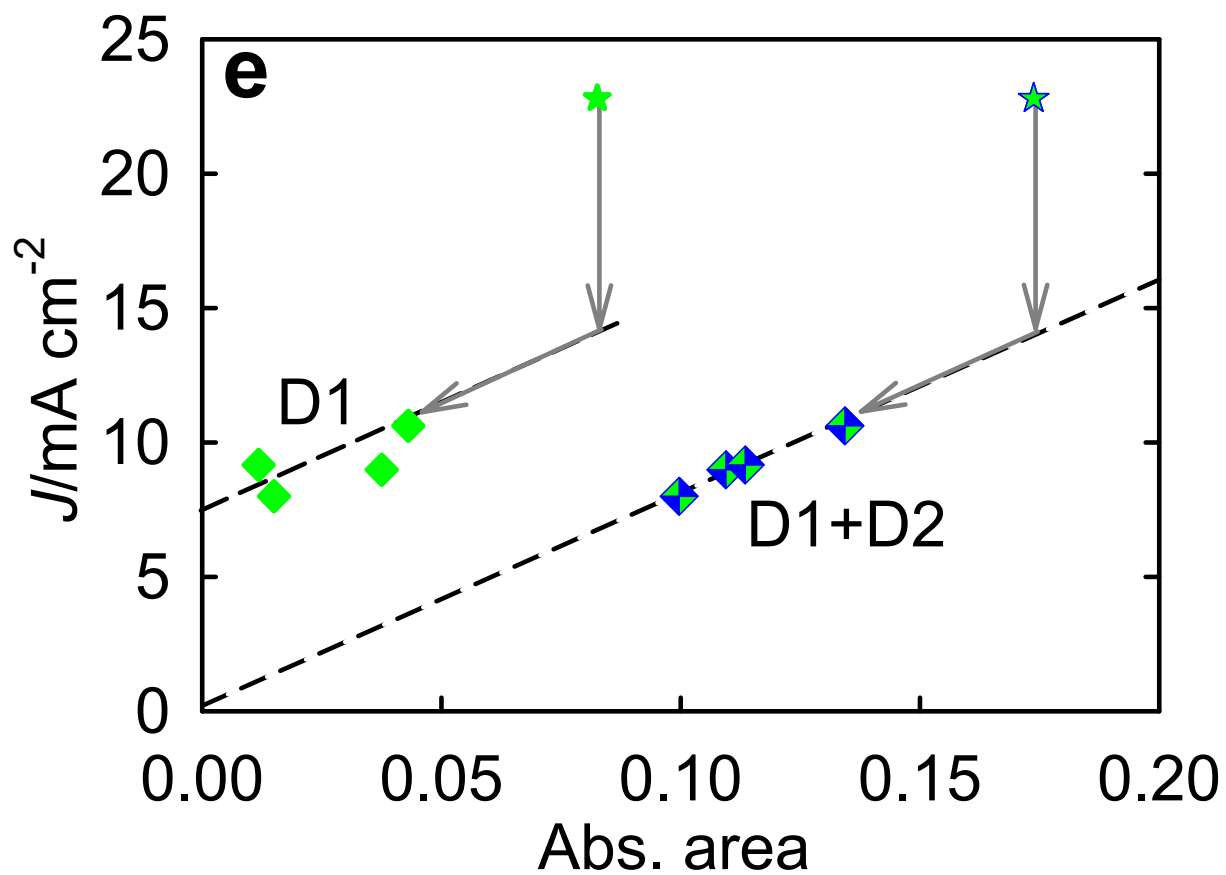
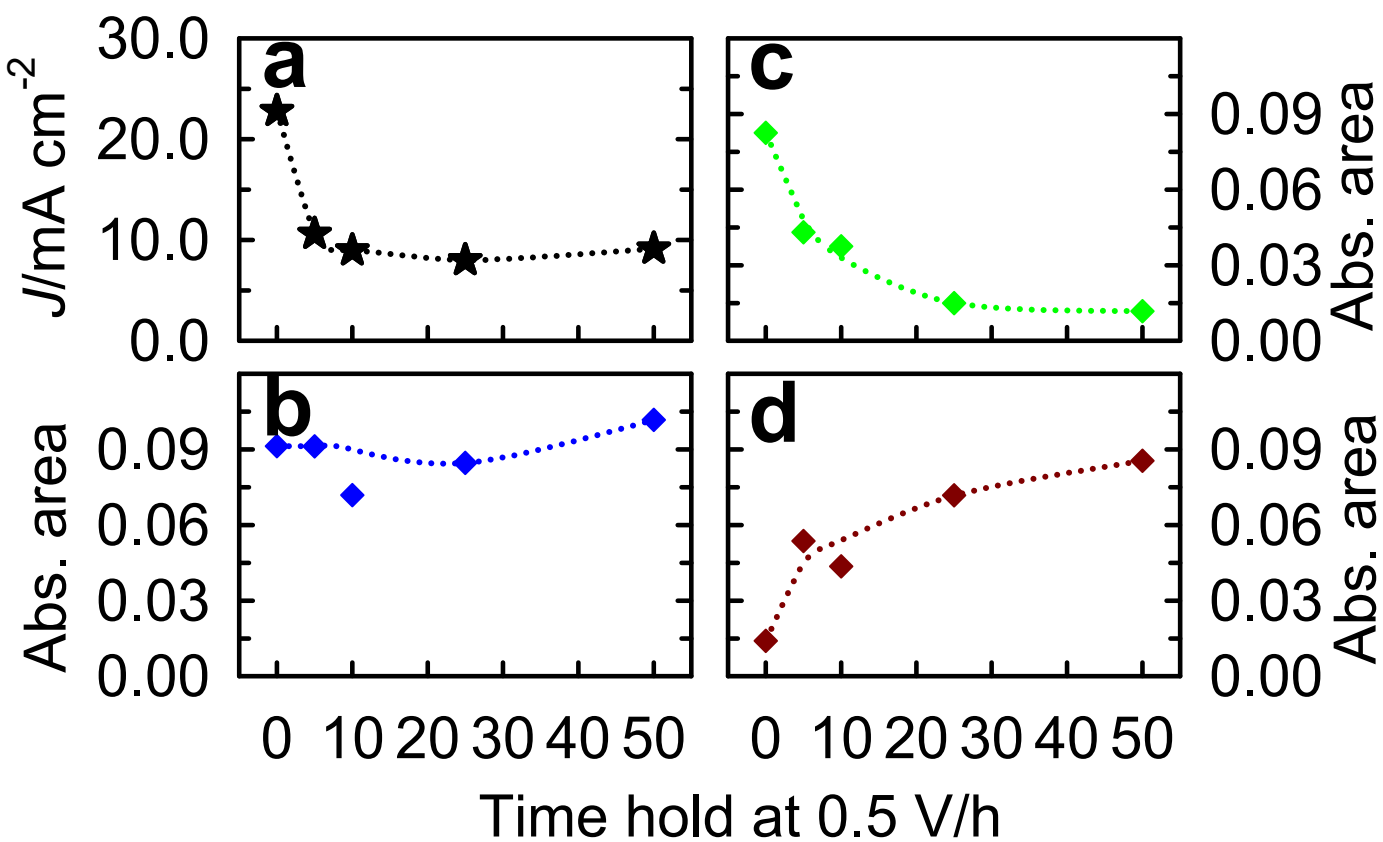
895



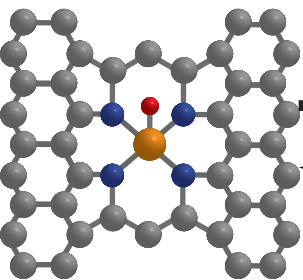






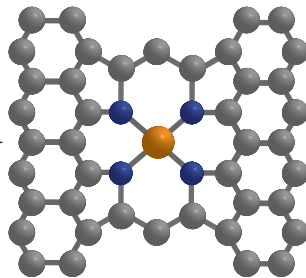


Site S1

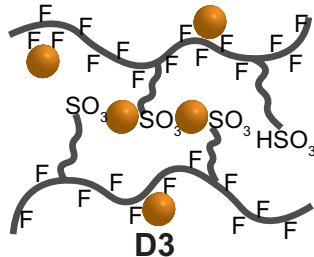


D1H (0.8 V) *ex situ*

Ar



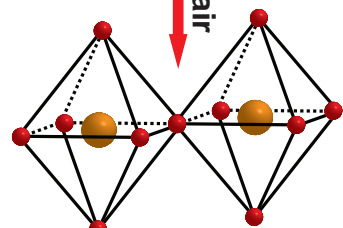
D1L (0.2 V)



D3

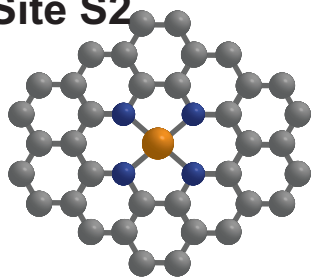
O₂

Expose to air



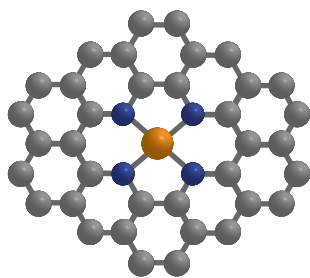
Fe₂O₃ clusters

Site S2



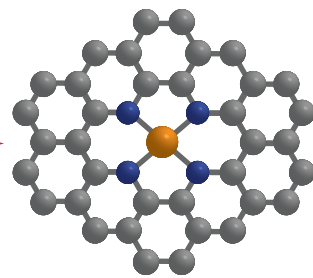
D2

Ar



D2

O₂



D2

